

AFRL-PR-WP-TP-2007-233

**HVEPS SCRAMJET-DRIVEN MHD
POWER DEMONSTRATION TEST
RESULTS (PREPRINT)**

**J.T. Lineberry, L. Begg, J.H. Castro, Ron J. Litchford,
and J.M. Donohue**



JUNE 2007

Approved for public release; distribution unlimited.

STINFO COPY

This work was funded in whole or in part by Department of the Air Force contract F33615-01-D-2109-0008. The U.S. Government has for itself and others acting on its behalf a paid-up, nonexclusive, irrevocable worldwide license to use, modify, reproduce, release, perform, display, or disclose the work by or on behalf of the U.S. Government.

**PROPULSION DIRECTORATE
AIR FORCE MATERIEL COMMAND
AIR FORCE RESEARCH LABORATORY
WRIGHT-PATTERSON AIR FORCE BASE, OH 45433-7251**

REPORT DOCUMENTATION PAGE					Form Approved OMB No. 0704-0188	
<p>The public reporting burden for this collection of information is estimated to average 1 hour per response, including the time for reviewing instructions, searching existing data sources, gathering and maintaining the data needed, and completing and reviewing the collection of information. Send comments regarding this burden estimate or any other aspect of this collection of information, including suggestions for reducing this burden, to Department of Defense, Washington Headquarters Services, Directorate for Information Operations and Reports (0704-0188), 1215 Jefferson Davis Highway, Suite 1204, Arlington, VA 22202-4302. Respondents should be aware that notwithstanding any other provision of law, no person shall be subject to any penalty for failing to comply with a collection of information if it does not display a currently valid OMB control number. PLEASE DO NOT RETURN YOUR FORM TO THE ABOVE ADDRESS.</p>						
1. REPORT DATE (DD-MM-YY) June 2007		2. REPORT TYPE Conference Paper Preprint		3. DATES COVERED (From - To) 01 August 2005 – 01 June 2007		
4. TITLE AND SUBTITLE HVEPS SCRAMJET-DRIVEN MHD POWER DEMONSTRATION TEST RESULTS (PREPRINT)				5a. CONTRACT NUMBER F33615-01-D-2109-0008		
				5b. GRANT NUMBER		
				5c. PROGRAM ELEMENT NUMBER 62203F		
6. AUTHOR(S) J.T. Lineberry (LyTec LLC) L. Begg (General Atomics) J.H. Castro (Pratt Whitney RocketDyne) Ron J. Litchford (NASA MSFC) J.M. Donohue (United Technologies Research Center)				5d. PROJECT NUMBER 3145		
				5e. TASK NUMBER 29		
				5f. WORK UNIT NUMBER 314529PL		
7. PERFORMING ORGANIZATION NAME(S) AND ADDRESS(ES) LyTec LLC Tullahoma, TN 37388 ----- General Atomics San Diego, CA 92186 ----- Pratt Whitney RocketDyne West Palm Beach, FL 33410				8. PERFORMING ORGANIZATION REPORT NUMBER ----- United Technologies Research Center Hartford, CT 06118		
9. SPONSORING/MONITORING AGENCY NAME(S) AND ADDRESS(ES) Propulsion Directorate Air Force Research Laboratory Air Force Materiel Command Wright-Patterson AFB, OH 45433-7251				10. SPONSORING/MONITORING AGENCY ACRONYM(S) AFRL/PRPE		
				11. SPONSORING/MONITORING AGENCY REPORT NUMBER(S) AFRL-PR-WP-TP-2007-233		
12. DISTRIBUTION/AVAILABILITY STATEMENT Approved for public release; distribution unlimited.						
13. SUPPLEMENTARY NOTES <p>Conference paper submitted to the Proceedings of the AIAA Plasmadynamics and Laser Conference. This work was funded in whole or in part by Department of the Air Force contract F33615-01-D-2109-0008. The U.S. Government has for itself and others acting on its behalf a paid-up, nonexclusive, irrevocable worldwide license to use, modify, reproduce, release, perform, display, or disclose the work by or on behalf of the U.S. Government.</p> <p>PAO Case Number: AFRL/WS 07-1252; Date cleared: 29 May 2007. This paper contains color.</p>						
14. ABSTRACT <p>The Air Force sponsored Hypersonic Vehicle Electric Power System (HVEPS) program was a research program to develop scramjet driven magnetohydrodynamic (MHD) power for an advanced high power, airborne electric power system. This program has been active for the past five years with various technical tasks being addressed that have encompassed engineering investigations of a myriad of technical issues related to airborne hypersonic MHD power system integration and operation. The integrated scramjet-driven MHD power demonstration ground test program was successfully accomplished in December 2006. The MHD power demonstration tests were conducted in the UTRC scramjet test cell wherein modifications to the test cell were made to install an in-line, direct fired MHD generator test article downstream of the facility's scramjet combustor.</p>						
15. SUBJECT TERMS Magnetohydrodynamic Generator, Hypersonics, Scramjet						
16. SECURITY CLASSIFICATION OF:			17. LIMITATION OF ABSTRACT: SAR	18. NUMBER OF PAGES 36	19a. NAME OF RESPONSIBLE PERSON (Monitor) Rene J. Thibodeaux 19b. TELEPHONE NUMBER (Include Area Code) N/A	
a. REPORT Unclassified	b. ABSTRACT Unclassified	c. THIS PAGE Unclassified				

HVEPS Scramjet-Driven MHD Power Demonstration Test Results

J. T. Lineberry*
LyTec LLC, Tullahoma, TN, 37388

L. Begg†
General Atomics, San Diego, CA, 92186

J. H. Castro‡,
Pratt Whitney RocketDyne, West Palm Beach, FL, 33410

Ron J. Litchford¶
NASA MSFC, Huntsville, AL, 35812

J. M. Donohue**
United Technologies Research Center, Hartford, CN, 06118

Abstract

Under the US Air Force sponsored Hypersonic Vehicle Electric Power System (HVEPS) program the authors' organizations are collaborating on research and development of scramjet driven magnetohydrodynamic (MHD) power for an advanced high power, airborne electric power system. This program has been active for the past five years with various technical tasks being addressed that have encompassed engineering investigations of a myriad of technical issues related to airborne hypersonic MHD power system integration and operation. In the latest effort of this program an integrated scramjet-driven MHD power demonstration ground test program was successfully accomplished in December 2006. The MHD power demonstration tests were conducted in the UTRC scramjet test cell wherein modifications to the test cell were made to install an in-line, direct fired MHD generator test article downstream of the facility's scramjet combustor. The heat sink 60° DWC MHD generator channel was situated within the bore of a 2.0 Tesla split-coil, superconducting magnet that was made available by NASA. The MHD power demonstration tests consisted of two series of scramjet firings on separate days at peak magnetic field strengths of 1.48 and 1.8 Tesla. In all tests, significant levels of MHD electric power were produced at different MHD generator resistive load settings. The peak MHD performance achieved at near maximum power operating conditions was a level of 14.8 kW of power electric output which was well within the range targeted by the HVEPS program. This paper presents the experimental data from the scramjet driven MHD demonstration tests and provides MHD performance analysis of these data in reference to scramjet combustion efficiency and plasma non-uniformity effects.

I. INTRODUCTION

In the early 1990's, considerable interest was regenerated on the potential use of magnetohydrodynamic (MHD) power generation and acceleration for application to advanced hypersonic vehicles and for re-entry control. Within this realm are works by the authors' and others on advanced magneto-plasma-aero flow and flight control concepts and lightweight MHD power systems for hypersonics.¹⁻⁹ These works have encompassed a myriad of novel ideas exploring the use of controlled MHD flow interaction with the plasma sheath that forms around a flight vehicle when flying at hypervelocity. Investigations have included analytical and laboratory research on aerodynamic drag reduction, thermal management of leading edge aero-heating, aero-braking/aero-steering, hypersonic inlet shock positioning control, MHD bypass assisted scramjet propulsion, and on-board high power systems. These advanced concepts and others have been topics for scientific evaluation under the banner of both the US Air Force and NASA hypersonic initiatives as well as within many international aerospace programs.

* President & CEO, Senior Member AIAA

† Manager, Space Power Division, Member AIAA

‡ Manager, DoD Strategy & Business Development, Member AIAA

¶ Propulsion Research Laboratory, Associate Fellow AIAA

** Research Engineer, Senior Member AIAA

In the actual field application of these future types of airborne Magneto-Plasma-Aerodynamic (MPA) systems there is the common requirement for an on-board compact, flight weight, high electric power source. In the case of surface electromagnetic flow/aero/thermal management for full-scale vehicles power needs on the order of megawatts will be required. For gross applications; such as, hypersonic inlet flowfield manipulation, MHD bypass scramjet propulsion, and for powering auxiliary systems; power demands in the 10's of megawatts are envisioned as being necessary. The overriding flight vehicle weight and volume requirements for an electric power system with a high power specific (MW/kg) and high power density (MW/m³) makes the MHD generator a leading candidate to meet these needs.

The initial works under the HVEPS program were directed at engineering evaluations of vehicle integration issues for different types of MHD power systems and their individual components based on current and advanced technology. The HVEPS flight mission for this system was directed by the AFRL and included the specification of vehicle flight at Mach 6 to 12 within an altitude range of 100,000 ft to 120,000 ft. The duty cycle demand for the power system was a power production level of 10 MW with multiple power bursts (up to 10 seconds duration) for an overall mission power-on time of 600 seconds. The system also had to have the capability of burst operation (turn-on and turn-off on demand) and; in addition to these, an overall power system weight (payload weight) of less than 10,000 kg was targeted.

Two concepts of MHD power system were screened in the early HVEPS studies. The first of these was a combustion-driven MHD pulse power system. This type of MHD power system is self-contained in that it is fired by an independent high pressure, high temperature combustor to produce a high velocity plasma, flow that drives the MHD generator. The self-contained combustion-driven MHD system is required to contain its own high energy fuel, oxidizer and ionization seed supplies. This type of high power density MHD generator is typical of conventional MHD technology and pulse power systems of this type have been fielded and produced electric power pulse of 20 to 500 MW.¹⁰⁻¹³ However; in past MHD research and development, all combustion-driven pulse power systems were ground-based and no constraints on system weight or size were required. The principal engineering efforts under the HVEPS program in its evaluation of this type of MHD system was that of packaging (i.e., minimizing system size and weight) to make the system compatible with the airborne platform.

The second MHD power system concept explored under HVEPS is illustrated in Figure 1. This system is a scramjet-driven MHD generator in which the MHD generator is directly integrated into the propulsion system flow path, downstream of the scramjet combustor. The scramjet-driven MHD concept was favored by the AFRL for further exploration based on the fact that the working plasma for the power system is generated from combustion of free stream air with conventional scramjet fuels. This aspect of this power system concept negates the requirement of to carry additional vehicle payload for the power system fuel and oxidizer. In principle, the high temperature plasma for the MHD process is produced by a combination of the compression (pre-heat) of the inlet air at hypersonic Mach number flight in conjunction with the scramjet's combustion heat release. As such, through the flight Mach number range and altitudes of interest it requires the addition of ionization seed material to produce a MHD compatible plasma flow and is it is subject to operation at flight Mach numbers above 6.0 when combustion is conventional jet fuel in air.

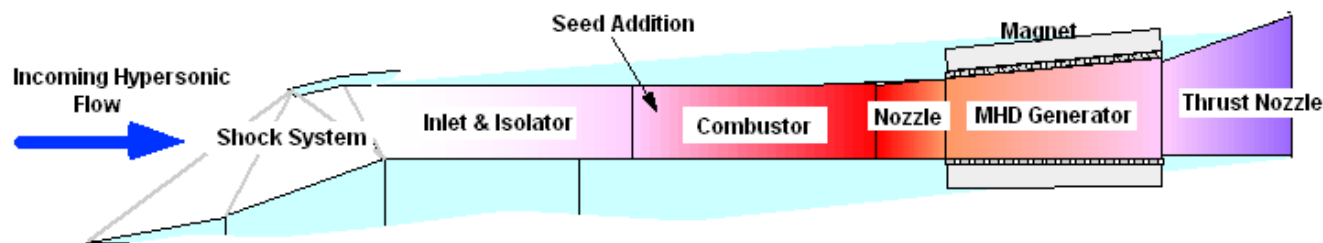


Figure 1. Scramjet-Driven Air Borne MHD Generator Concept

From tradeoff evaluations and engineering studies of these two MHD power system concepts that were completed in the HVEPS initial studies, it was concluded that either of these systems could be designed to meet the AFRL mission as stated and their further development was pursued under HVEPS. The self-contained combustion-driven MHD power system's dry weight is lighter and its volume is less than the scramjet-driven MHD power system through its use of energetic fuels (e.g., C₂N₂, Al) to achieve extremely high plasma conductivity and MHD power density. However, the scramjet-driven MHD power system can be uniquely integrated into the scramjet propulsion flow path and this system has the advantage of not requiring extra fuel and oxidizer tankage. The general conclusion drawn from comparing these two

MHD power systems is that which one is most appropriate for the airborne application is dependent on duty cycle demand for the power needs. Whereas, the self-contained combustion driven MHD power system has the lighter dry weight (~50% less) because it is a higher power density machine; for power-on times in excess of approximately 600 seconds – its take-off weight (dry weight plus fuel and oxidizer payload) will be greater than that for the scramjet driven MHD power concept.

A summary of the findings of the complete HVEPS program is too extensive for inclusion herein. For more information, references 1 and 2 can be reviewed which were precursor technical papers to this current one. One overriding outcome of the previous HVEPS work that was directed by the AFRL management was the need to provide a definitive demonstration of the ability to produce MHD power with a scramjet engine. With this need in-mind, the HVEPS program set in place a focused task under AFRL issued HVEPS delivery orders, to conduct a “scramjet driven MHD power demonstration test”. This work was undertaken as a collaborative effort by the organizations of the authors.

The demonstration testing was successfully completed in December of 2006. The results of that testing are the technical subject addressed herein.

II. HVEPS SCRAMJET-DRIVEN MHD POWER DEMONSTRATION TEST

Although the scramjet-driven MHD power system has been considered in past MHD works, to-date only the HVEPS program has conducted the detailed conceptual analysis as needed to conclude the viability of this concept. There remained a technical concern that the supersonic combustion process of the scramjet engine may not be capable of producing a plasma with the high electrical conductivity and with a flow structure that was uniform enough to promote an effective/efficient MHD power production process. With this issue in mind, the reported work under HVEPS concentrated on assembling a moderate size, scramjet test cell to provide a ground test bed for conduct of a proof-of-concept demonstration test for scramjet-driven MHD power generation.

To achieve this hypersonic MHD power demonstration test, the HVEPS program prime contractor, General Atomics, assembled a team consisting of the following organizations and their responsibility; Pratt&Whitney (P&W) – scramjet technology lead, United Technologies Research Center (UTRC) – scramjet test cell and test conduct lead, LyTec LLC – MHD generator test article components lead, NASA MSFC – provision and operation of the superconducting magnet test article.

The scramjet test cell of UTRC exists and it has been used extensively in AFRL sponsored scramjet development research. The scope of work under the HVEPS program was to modify the operation of the existing test cell to provide simulation of Mach 8.0 flight; design and fabricate a geometrically compatible MHD generator test article (including all its support components), install the generator in the test cell in-line with the scramjet exhaust, and conduct demonstration experiments with the goal of MHD electric power production. The successful achievement of this goal was to demonstrate proof-of-concept for scramjet-driven MHD power system to set the stage for more aggressive development of this concept for future fielding.

A. Scramjet Driven MHD Power Demonstration Test Facility

Detailed descriptions of the UTRC scramjet test facility and the design of the MHD generator components/hardware items that formed the MHD power demonstration test bed can be found in References 1 and 2. Only a brief description is provided below.

Scramjet Test Bed. The UTRC scramjet combustor test rig (Test Cell 5) can simulate conditions for the flight regimes of interest for hypersonic vehicles (Mach numbers of 4.0 to 8.0, altitude > 100,000 ft, dynamic pressures up to 1,250 psf). The facility operates as blowdown tunnel in the direct connect mode with a vacuum air ejector exhaust system that holds back pressure to about 4.0 psia in the downstream exhaust quench tank. Combustion efficiencies of between 70 and 95% are typical for the rig depending on test condition and fueling configuration. The nominal total throughput for the combustor test rig is on the order of 3.0 lb/sec, depending on test condition and fueling; operational times of up to forty seconds are achievable.

The UTRC scramjet combustor test article is supplied with a hydrogen vitiated, high pressure, high temperature air stream, using air vitiation at various degrees to provide the needed free stream total temperature simulation. The scramjet combustor can be fueled with hydrogen or a variety of gaseous or liquid hydrocarbon fuels that can be heated and endothermically cracked to simulate the fuel state at the flight condition corresponding to engines that use fuel for structural cooling.

Figure 2 is a schematic of the scramjet test rig with notation of all the major existing components and feed systems. At the exit plane of the combustor the combustion reaction are quenched by a series of water spray bars before the flow enters the calorimeter duct. Figure 3 is a photograph of the combustor test article with the top wall section that contains the primary fuel injector flame holder region removed. The scramjet combustor test article is constructed from AISI 4130 thick steel plate heat sink walls with water cooling introduced in critical heat flux areas. Windows in the piloting region and near the exit of the combustor are available for monitoring flame stability and for implementing optical diagnostics.

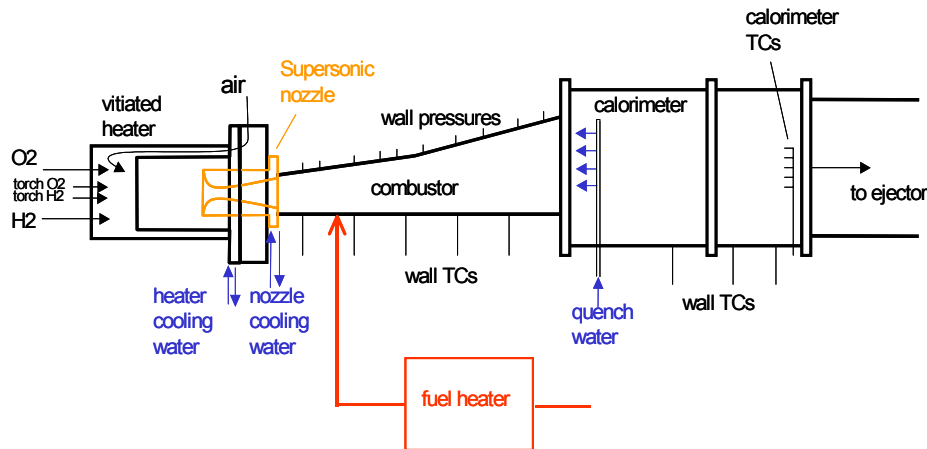


Figure 2. Schematic of UTRC Scramjet Combustor Rig

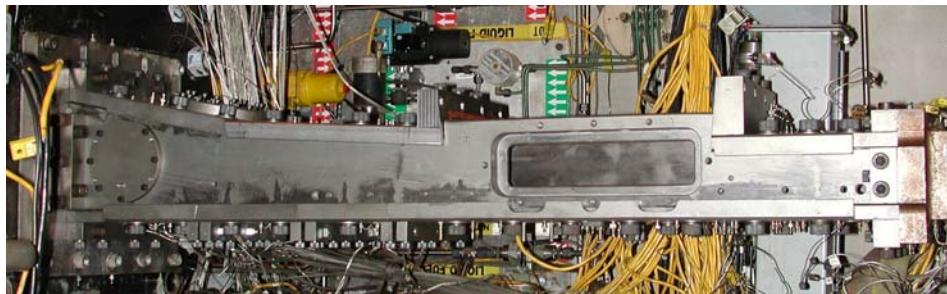


Figure 3. Photograph of UTRC Test Cell 5 Scramjet Test Article

Standard instrumentation is used to characterize the test conditions and combustion process and this will be maintained consistent for the HVEPS demonstration test. Measurements include input flow rates of air, vitiator hydrogen and oxygen to determine oxygen fraction, combustor fuel flow, input total temperature, static pressure distributions, and embedded wall thermocouples to monitor heat losses. Combustor fuel flow rates set the combustor equivalence ratio. Additional measurements of quench water flow rates and the rig's wall heat losses allow calorimetric determination of combustion efficiency.

The major modification to the test bed that was required for HVEPS testing was the modifications to accommodate ionization seed injection. This required providing a penetration in the backplate of the pre-heater to implement a seed injection port. Other laboratory modifications were required to accommodate operational and safety issues related to test operations in a high magnetic field area. In general, these consist of assuring personal safety and that any possible magnetic field interference with controls and/or instruments is accounted, and if so, these are to be repositioned outside the high magnetic fringe field areas.

NASA Split Coil Superconducting Magnet. A small 3.0 Tesla superconducting magnet was made available on loan to HVEPS through contractual arrangements were made between General Atomics and NASA under a NASA Space Act Agreement. This agreement provided HVEPS with access to the NASA magnet and provided for experienced NASA staff to assist in its operation during the MHD power demonstration testing.

Figure 4 is a photograph of the NASA super-conducting magnet. The magnet is of split-coil design configured of two independent circular NiTi superconducting coils separated by a spacer. Each coil is contained within a liquid helium dewar. The design specifications for the magnet was capability of producing a peak field of 3.0 Tesla in the center region between the coils for a spacing of six inches between the coil dewars when powered at 90 Amps. The central field area is twelve inches in height with a bore length of thirty-five inches. The spacing between the coils dewar faces that was required to accommodate the demonstration test MHD generator channel was ten and one-half inches.

The magnet set-up as shown in Figure 4 was used to provide measurement of the magnetic field profile. The results of those measurements are shown in Figures 5. The increased coil spacing required to accommodate the HVEPS MHD channel lends a peak magnetic field strength in the center of the magnet at approximately 2.2 Tesla.

MHD Generator Channel and Sub-Systems. The MHD generator channel and its subsystems were mechanically designed and fabricated by LyTec. These include five specific pieces of hardware, i.e., the ionization seeding system, the resistive load bank, the channel upstream transition duct, the MHD generator channel, and the downstream diffuser.

NaK Seed Injection System. Ionization seeding for the scramjet-driven MHD demonstration test was accomplished by the injection of liquid NaK into the backplate of the UTRC pre-heater. NaK is a eutectic consisting of approximately 80% potassium and 20% sodium. It exists in liquid form at room temperature and has flow properties quite similar to water. However, there are materials handling safety issues with use of NaK since it is highly caustic alkali metal and burns on contact with moisture.

All NaK system plumbing components were stainless steel to avoid corrosion. The system consisted of a high pressure NaK reservoir that was pressured to operating pressure with Argon. In operation, a control valve was opened allowing the liquid NaK to flow into the pre-heater through a barbotage type dispersion injector tube. The barbotage injection tube consists of an inner tube which is feed with high pressure Argon and an outer annulus which provides the flow passage for the liquid NaK. Final fabrication and assembly of the seeding system was completed at UTRC as well as the pre-heater modifications required to accommodate the injector, system structural support and safety containment.

Resistive Load Bank. Electric power produced in the scramjet-driven MHD power demonstration test was consolidated and dissipated in a remotely located resistive load bank. The load bank was of simplistic design consisting of twelve nichrome 10 kW resistive heating elements of 5.8 Ohms each and rated at 40 Amps for continuous operation. The resistive elements could be wired in series and parallel circuits to provide a range of MHD generator loading from 0.5 to 66 Ohms which covered most of the anticipated operational generator load line. Buss work for the MHD generator power leads was provided at the load dump for power consolidation.

MHD Generator Channel and Flow Components. The MHD generator channel and its mating flow components consists the ductwork combination of the upstream transition duct, the active generator channel, and the downstream diffuser with an electrical isolation flange. These flow components are identified in the assembly drawing of Figure 6.

The upstream transition duct that mates directly to the scramjet combustor exit and served to provide for a smooth turning of the scramjet 11 degree upper wall back to near horizontal to match the MHD channel's internal flow passage divergence. The transition duct was of a sufficient length of flow duct upstream of the generator channel to assure the location of the active MHD channel was centered in the magnetic field (see Figure 5).



Figure 4. NASA Split-Coil Superconducting Magnet

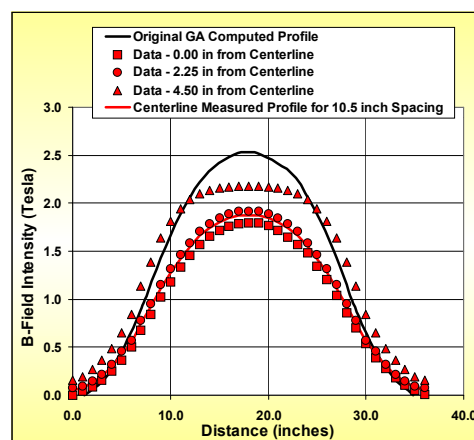


Figure 5. NASA Split-Coil Superconducting Magnet Axial Magnetic Field Profiles

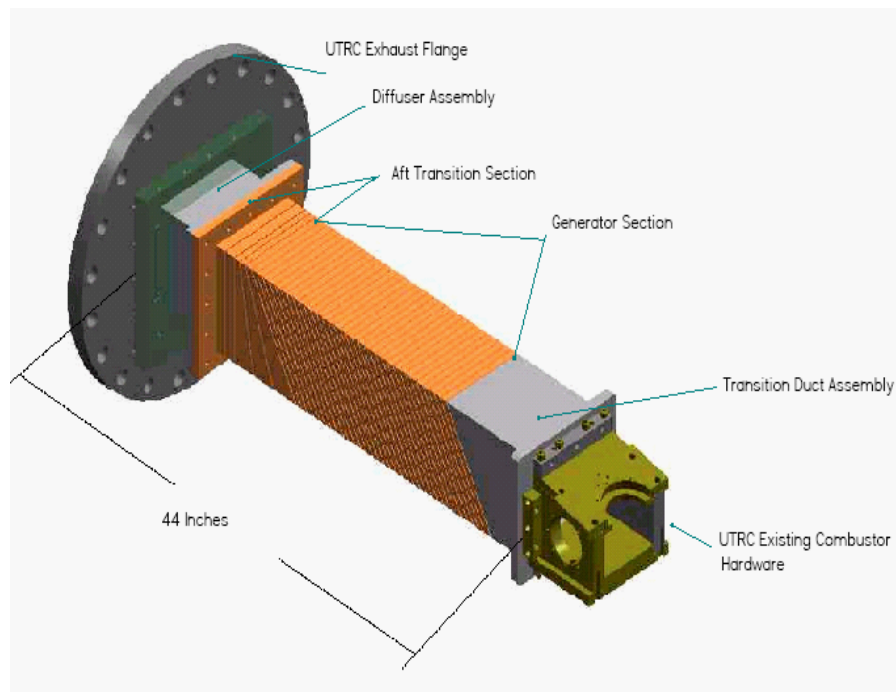


Figure 6. Assembly Layout of the MHD Generator and Mating Flow Path Components

The transition duct was constructed from welded austenitic stainless steel (non-ferromagnetic) so as to not distort the magnetic field distribution. Its design was such that the downstream face of the duct was slanted at 30 degrees from the vertical to match the diagonalization angle of the MHD generator channel.

The heat sink MHD generator design is typical to that of a diagonally conducting wall (DCW) configuration with window frame electrode construction. A photograph of the MHD generator channel with attached upstream transition duct and mounted in its phenolic lifting tray/channel beam support is shown in Figure 7. Features of the channel design can be inferred from this photograph including copper heat sink electrode material, the electrode diagonalization, and discrete electrode segmentation that is visible.

There were a total of 33 active 60 degree oriented electrodes in the assembled generator channel over a total active length of 23.39 inch; the resultant electrode pitch is 0.708 inches. The first five and last five active electrodes include power takeoff lugs on their upper surface for power consolidation to the load dump. Each electrode was equipped with instrumentation lugs on the sidewall above the lifting tray to allow for the measurement of voltage distribution.



Figure 7. Photograph - Assembled MHD Generator Channel

Diffuser and Downstream Electrical Isolation Flange. The diffuser re-expands the flow stream exiting the generator channel for eventual shock down to back pressure conditions at the downstream breach entrance. With powered operation of the MHD generator, the diffuser end of the flow train is at high potential to ground and must be electrically isolated. The diffuser section was outside the magnetic field so it was constructed from welded carbon steel flat plate with 1.0° diverging internal walls. Electrical isolation was provided by a one inch thick phenolic isolation piece between the downstream diffuser flange and the breach. Fastening of the phenolic isolation piece is by separate bolting of the diffuser external flange to helicoils in the phenolic and then independent bolting of the phenolic to the breach entrance flange through countersunk holes.

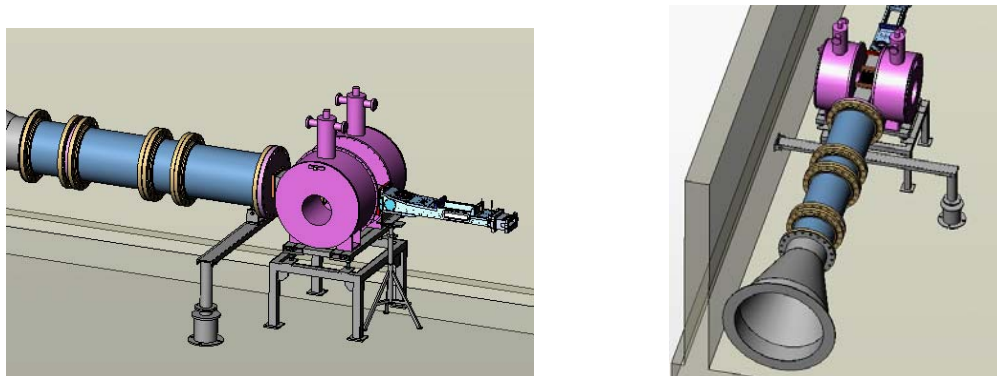


Figure 8. UTRC 3-D CAD Layout of the Scramjet-Driven MHD Assembled Test Rig

Assembled MHD Test Train. Fabrication of all components for the scramjet MHD power demonstration test and all needed test facility modifications were accomplished as planned and the finished test train was assembled and readied for testing in late November of 2006. The assembly of the test train is most easily viewed by the pre-assembly 3-D schematic shown in Figure 8. This artists' sketch shows the in-line mating of the MHD generator to the scramjet engine and exhaust breach with the generator channel situated laterally inside the superconducting magnet and orthogonal to the direction of the magnetic field between the coils.

Geometric and physical design specifications for the MHD generator section of the overall test train are summarized in Table I. The MHD generator section was affixed to the scramjet exit flange and to the breach flange such that it was totally self-supporting with no physical contact to the superconducting magnet structure. It was centrally positioned within the superconducting magnet bore in both the horizontal and vertical directions. The wall thickness of the channel was approximately 1.25 inches on each side to provide the required heat sinking mass to allow for ten seconds of hot firing.

TABLE I

HVEPS Demonstration Test MHD Generator Design Parameters

Train Internal Flow Loft	Specification
Scramjet Combustor Outlet Height (cm)	13.82
Scramjet Combustor Outlet Width (cm)	15.24
Inlet Transition Section Length on CL (cm)	23.74
MHD Generator Inlet Height (cm)	14.95
MHD Generator Inlet Width (cm)	15.24
MHD Generator Length (cm)	59.28
MHD Generator Exit Height (cm)	15.91
MHD Generator Exit Width (cm)	15.24
Trans & Extension Section Length (cm)	19.45
Diffuser Entrance Height (cm)	16.25
Diffuser Entrance Width (cm)	15.24
Diffuser Exit Height (cm)	16.70
Diffuser Exit Width (cm)	15.88
MHD Test Train Total Length (Entrance to Exit) (cm)	111.76
Physical Design Features	Specification
Configuration	Diagonal Conducting Sidewall (DCW)
Electrode Design	Window Frame (Inclined 60°)
Electrode Material	1/2 inch Thick OFHC Copper Plate
Insulator Material	1/8 in Thick Cotronics Ceramic Impregnated Gasket (360-1EHS)
Diagonalization Angle	60 degrees (from horizontal)
Loft Divergence	+/- 0.5 Degree Upper and Lower Wall Zero Divergence of Sidewalls
Number of 60 Degree Electrodes	33
Electrode Pitch (cm)	1.80

Each electrode was separated by 0.125 in thick interelectrode insulators composed of a commercially available ceramic impregnated gasket with a dielectric rating of 1,000 V/mil. Interelectrode isolation was hand checked during assembly and after insulation using a megar setting of 1,000 Volts – electrical isolation between all adjacent electrodes was recorded at over 500 megaohms.

Figure 9 is a photograph of the final assembled apparatus. The view of this photograph is for the upstream/scramjet end of test train showing the mating of the scramjet exit to the entrance of the MHD generator channel. The superconducting split coil magnet and its support structure are visible in Figure 9.

Loading and Electrical Instrumentation. The electrical hookup of the channel including voltage instrumentation leads and the generator power take-off (PTO) wiring to the load dump was completed by UTRC upon final assembly. The resistive load dump was remotely positioned in the test bay downstream of the MHD generator.

The data system used for HVEPS demonstration tests includes both the standard facility instrumentation as well as a high voltage, high speed data system used for the MHD power measurements. Standard facility instrumentation was used to characterize the test conditions and the combustion process.

MHD generator electrical measurements were made with a DATAQ model 730EN high speed, high voltage data

system configured for 1 kHz data rates with 14 bit resolution. Differential voltage at seven axial locations along the MHD channel was measured between groups of electrodes of the MHD channel and power take-off leads. The general scheme for the high voltage and current measurements is illustrated in Figure 10. Voltage across the load dump was determined from the sum of the differential voltage measurements along the MHD channel

A portable, Fluke multi-meter data recorder was also used to measure and record voltage across the load dump during testing. This meter served as a back-up to the DATQ system and voltage measurement from the meter was compared with the measurements made on the DATAQ system as part of immediate post-test activities.

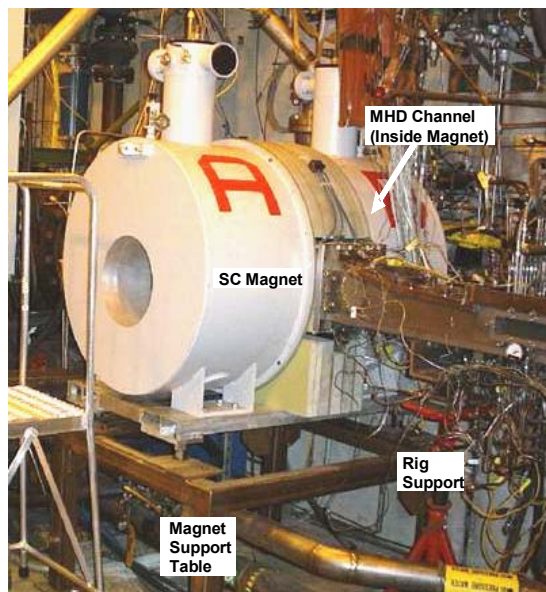


Figure 9. Photograph of Assembled Scramjet MHD Test Bed Prior to Testing

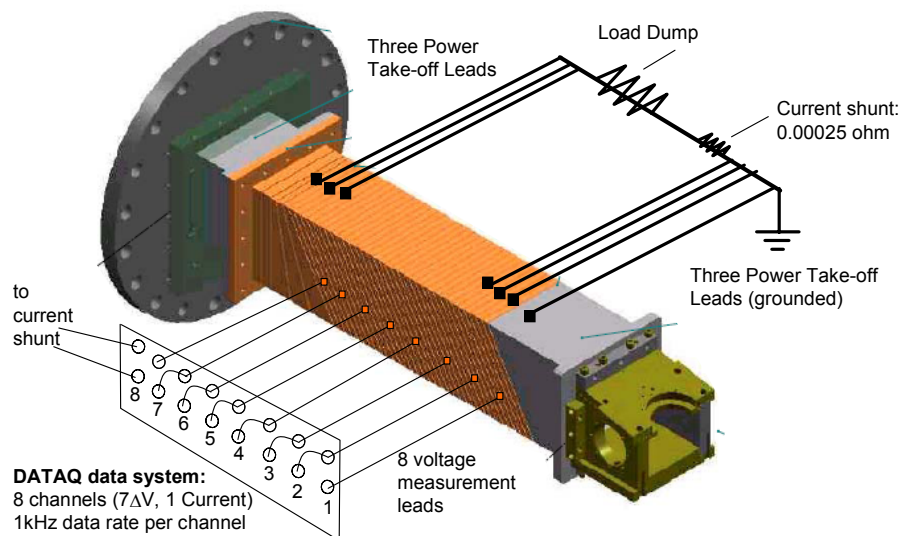


Figure 10. Illustration of MHD Generator Electrical Hook-up and Instrumentation

III. TEST OPERATION AND PERFORMANCE ISSUES

The fundamental objective of this HVEPS project was to demonstrate the ability to produce MHD electric power using scramjet combustion. With this focused goal set for the project, the experimental phase of the work consisted of only a few tests to map the MHD generator operational loadline and define electric power production. The specific test plan for the experimental phase was formalized by the HVEP's team with this focused objective in mind.

Design and pre-test analysis of the scramjet combustion that was conducted in the early phase of the project provided theoretical validation that the elevated combustor exit temperature needed to produce a seeded plasma with a sufficient electrical conductivity and MHD power density was plausible with operation of the scramjet at its simulated Mach 8 test condition. This was the higher end of this scramjet test rig's capability. To achieve the high Mach free stream simulation and the high combustor exit temperature that was needed, test simulation required introduction of oxygen enrichment to the pre-heater exit flow and then subsequent near stoichiometric combustion in the scramjet engine.

Table II provides a tabulation of the targeted scramjet combustor operating point that was targeted for the MHD power demonstration testing. This table was generated using calculation from PWR's RASCAL code in conjunction with LyTec's thermochemical code for the needed calculation of plasma electrophysical properties. The scramjet combustor fuel choice for this demonstration test was preheated ethylene. This fuel is used to provide simulation of higher order gaseous hydrocarbons from thermally cracked JP-7.

Table II is structured as a function of combustor efficiency for a specified level of oxygen enrichment of 35%. Experience in operation of the scramjet test cell infers that overall combustion efficiency between 85% and 95% should be achievable at this MHD demonstration test condition. In order to provide verification of this, the MHD demonstration test condition was successfully run in March of 2006 in a UTRC baseline test series to provide a checkout of the operation of the rig prior to initiating actual work on laboratory preparation for the MHD demonstration test. The calorimeter data from the baseline test indicated an overall mean combustion efficiency of 84% was achieved.

TABLE II.
Scramjet-Driven MHD Power Demonstration Test Targeted Operation

PARAMETER	75% Efficiency	85% Efficiency	95% Efficiency
Pre-Heater H ₂ Flow	0.031 kg/sec	0.031 kg/sec	0.031 kg/sec
Air Flow	0.595 kg/sec	0.595 kg/sec	0.595 kg/sec
O ₂ Enrichment Flow	0.659 kg/sec	0.659 kg/sec	0.659 kg/sec
Seed (NaK) Flow	0.038 kg/sec	0.038 kg/sec	0.038 kg/sec
Scramjet Inlet Total Pressure	21.61 Atm	21.61 Atm	21.61 Atm
Scramjet Inlet Total Temperature	2,245K	2,245K	2,245K
Scramjet Combustor Fuel Flow (ethylene)	0.160 kg/sec	0.160 kg/sec	0.160 kg/sec
Scramjet Total Throughput	1.483 kg/s	1.483 kg/s	1.483 kg/s
Scramjet Exit Total Pressure	2.469 Atm	2.355 Atm	2.374 Atm
Scramjet Exit Total Temperature	2,849K	2,923K	2,985K
Scramjet Exit Static Pressure	0.267 Atm	0.279 Atm	0.289 Atm
Scramjet Exit Static Temperature	2,349K	2,444K	2,522K
Exit Velocity	1,949.5 m/s	1,968.6 m/s	1,981.2 m/s
Exit Mach Number	2.116	2.086	2.055
Channel Entrance Electrical Conductivity	4.75 S/m	8.06 S/m	11.99 S/m
Channel Entrance Electron Mobility	1.182 T ⁻¹	1.205 T ⁻¹	1.214 T ⁻¹
Channel Entrance Faraday MHD Power Density Parameter	4.51 Mw/m ³ /T ²	7.81 Mw/m ³ /T ²	11.76 Mw/m ³ /T ²

The quality of the plasma exiting the scramjet combustor is indicated in Table II by the electrophysical properties (conductivity and mobility) and the ideal MHD power density parameter. The plasma MHD power density parameter is defined normalized with respect to magnetic field intensity as,

$$P_d = f \frac{\sigma u^2}{4}, \quad (1)$$

where σ is the electrical conductivity, u is velocity, and f is a variable functional dependent on Hall parameter and the MHD generator loading configuration. The Faraday MHD power density parameter (i.e., $f = 1$) is an indication of the ideal MHD power production capability of the dynamic plasma. It is notable in Table II that the plasma electrical conductivity varies by a factor of over 2.5 over the combustor efficiency range. Consequently, achieving as high a

combustion efficiency as possible was a key element in this test to demonstrate significant MHD electric power extraction.

The diagonal MHD power density parameter accounts for the actual diagonalized loading configuration used in the MHD generator channel final design. The B-field normalized, diagonal power density is defined as follows,

$$P_d = \frac{(\beta - \Phi)^2}{(1 + \beta^2)(1 + \Phi^2)} \frac{\sigma u^2}{4}, \quad (2)$$

where β is Hall parameter and Φ is the orientation of the diagonal electrical field as determined by the diagonalization angle (i.e., $\Phi = \tan E_y/E_x$).

The design level of inlet conductivity and diagonal power density for the MHD generator are shown on Figure 11. The design point selected for use in the MHD channel final mechanical design was that of combustion with an oxygen enrichment level of 34.5% at 85% combustion efficiency. One can see in Figure 11 that the same level of conductivity and diagonal power density can be achieved at lower oxygen enrichment when the combustion efficiency is elevated above the 85% threshold. Operation at lower oxygen enrichment is a less stressful situation on the heat sink hardware.

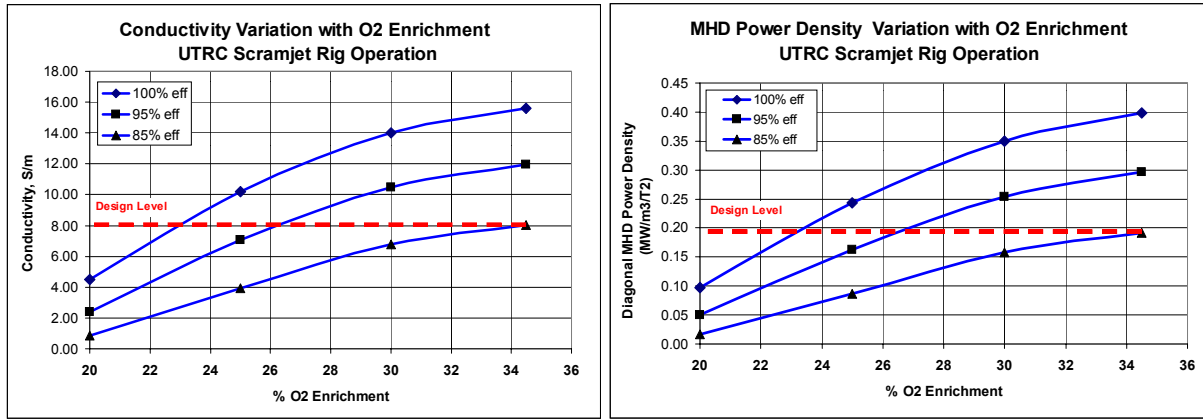


Figure 11. Plasma MHD Performance Parameters as a Function of Pre-Heater Oxygen Enrichment

In addition to the ideal level of plasma electrical conductivity and MHD power density as tabulated in Table II, the uniformity of the flow field exiting the scramjet combustor is also an extremely important characteristic for maximizing the ability to make MHD power. Non-uniform profiles of temperature, pressure and species concentration lower mean conductivity to an effective value related to profile shape and the large gradients near the walls introduce boundary layer voltage drops which dissipate power and reduce power output. A standard measure of plasma non-uniformity is the classic Rosa G-factor¹⁴ defined in accordance with the following,

$$G = \left\langle \sigma \right\rangle \left\langle \frac{1 + \beta^2}{\sigma} \right\rangle - \left\langle \beta \right\rangle^2, \quad (3)$$

the bracketed symbols around expressions indicated the integrated average of the quantities within over the local cross-sectional area of the plasma. In general, for a totally uniform flow structure (plug flow), the integration terms are constants and the G-factor degenerates to 1.0. That represents an ideal situation. Introduction of real flow structure with non-uniformities arising from boundary layer effects and in the scramjet case, non-uniform mixing and species burnout; the G-factor is greater than 1.0.

Introduction of plasma non-uniformity (in the form of Rosa G-factor) into the power density expression of Equation 3 produces the following expression for diagonal MHD power density,

$$P_d = \frac{(\beta - \Phi)^2}{(G + \beta^2)(G + \Phi^2)} \frac{\sigma u^2 B^2}{4} \quad (\text{Wt/m}^3), \quad (4)$$

In terms of power degradation due to flow field non-uniformity, the plasma MHD power density is seen to be strongly inversely proportional to the G-factor.

Plasma non-uniformity was an unknown factor for the combustion gas flow field exiting a scramjet combustor. Undoubtedly, significant flow non-uniformity can be anticipated from the supersonic combustion process and from the oblique shock train. Furthermore, the UTRC scramjet combustor test article was not designed with control over this characteristic as a criterion.

Indication of the exit flow non-uniformity for this test rig and its configuration for the MHD power demonstration test was evidenced by the 3-D combustion calculations that were performed by PWR in their combustion CFD analysis of the test condition. Figure 12 shows results from those calculations which are half-plane of symmetry; temperature, oxygen and fuel concentration contours at successive axial calculation stations extending from the fuel injection region to the exit.

The final exit contours represents computed conditions entering the MHD generator channel. Noticeable temperature non-uniformity was predicted in these results with elevated temperature in the core and reduced temperatures near the walls and in the upper central region. Regions of elevated fuel species concentration exist along the vertical wall and bottom corner and free oxygen concentration is elevated in the top central region. The CFD results of Figure 12 were encouraging since these indicated a combustion efficiency of 90% (in terms of burnout) and a mean global temperature of 2,450K.

In terms of the pre-test estimated MHD generator performance for the HVEPS demonstration test, LyTec performed parametric type MHD generator calculations during the design phase of the project. These calculations were based on operation of the scramjet combustor at the targeted flow rates for the baseline test and variable levels of combustion efficiency. General scramjet operation and generator inlet plasma dynamic flow and electrical properties derived from that work are specified in Table II.

The physical design of the MHD generator test article was predicated on design calculations for an optimistic G-factor of 2.0. Consequently, the targeted maximum electrical output power going into the actual scramjet-driven MHD demonstration test was 35 kW at 2.0 Tesla operating condition. It was planned for the actual demonstration test to implement mapping of the actual generator performance that was measured across the major portion of the loadlines through repeated testing as is possible; to define the actual level of non-uniformity and combustion efficiency experienced.

III. HVEPS SCRAMJET MHD POWER DEMONSTRATION TEST OPERATIONS

The scramjet MHD power demonstration tests were conducted on consecutive days during the late night shift. Night testing was implemented so that the high magnetic field would not be present in the facility and its surroundings during daylight hours for personnel safety. In general, the magnet field was energized prior to actual test conduct which required several hours due to the magnet controllers pre-set current ramp rate. Pre-test activities required approximately eight to ten hours to complete. Turn around time between consecutive tests was mostly dependent upon the amount of time required for a quick assessment of facility and MHD electrical data by UTRC and LyTec staff. This was on the order of two hours at the most.

UTRC scramjet facility operating conditions that were set for all MHD power demonstration tests are summarized in Table III. These set conditions were near identical to those run in the spring of 2006 in the baseline test series to verify operation at the Mach 8 test condition. Measured combustion efficiency in the baseline test was determined to be 84.1%

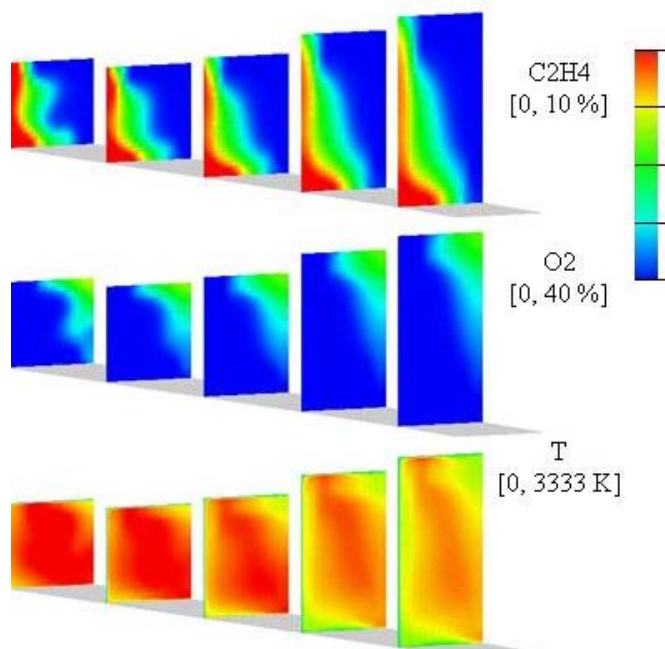


Figure 12. PWR CFD Computed Contours of the Flow Exiting the UTRC Scramjet Test Article

Table III
HVEPS Scramjet MHD Power Demonstration Test Set

inlet	O ₂ Concentration, %	35	
	Inlet P (psia).....	4.07	
	Inlet T (R)	1,640	
	Inlet V (ft/s)	6,700	
	Inlet total P (psia)	317	
	Inlet total T (R)	4,044	
	Air flow rate, lbm/s	2.83	
	W air	1.308	→ Wair=1.32 pps
	W O ₂	1.449	→ WO ₂ =1.48 pps
	W H ₂	0.069	→ WH ₂ =0.0705 pps
exit	Ethylene flow rate, lbm/s	0.35	→ Wethylene=0.35 pps
	η _{comb} %	85	→ η _{comb} @ 84.1%
	Total flow rate (air+fuel) lbm/s	3.18	
	Outlet Area, in ²	32.64	
	Static T (R)	4,444	
	Static P (psia)	4.1	→ Tt exit = 4,425R
	V (ft/s)	6,549	
	Outlet Mach Number	2.09	
	Total P (psia)	35.6	
	Total T (R)	5,288	
NaK seeder	NaK Flowrate (lbm/s)	0.085 (3% of air)	
	Argon Atomization (lbm/s)	0.060	

Run 195.1 Baseline Test
35% O₂ air and Phi=0.98
Completed March 2006

nominal from analysis of test rig calorimetry data. Only slight differences in the flows from the baseline test condition were instituted. The baseline tests did not include NaK seed injection, whereas, the MHD power demonstration tests employed seeding at approximately 2.5% of the total flow.

The MHD power test operating sequence is summarized in Table IV. The test sequence proceeds as follows: establish light off of the pre-heater (hold briefly to verify stability); light off of the scramjet (initiate ethylene fuel injection and hold briefly to verify burn stability); turn-on NaK injection; hold condition for three seconds of MHD power generation; turn-off NaK injection simultaneously with scramjet combustion (terminate ethylene fuel injection); purge residue NaK from its system feed lines with argon; and conclude the experiment with purge of the entire test train with cooling air and a sustained low flow of NaK argon purge until flow train cools (up to 10 minutes).

A total of seven MHD powered tests were accomplished in two series conducted on consecutive days. Table V provides a tabulation of the testing with MHD generator setup conditions and general comments. The MHD tests are referred to in consecutively order (1 through 7) in terms of when they were conducted in sequence. (UTRC test numbering is indicated in parentheses.)

All MHD power tests were visually observed by the test crew using remote video monitors in the control room and each test was also video recorded for archives. Video cameras were located inside the test bay with the recording camera focused on the scramjet view ports. Two view ports were available on the scramjet rig; a rectangular side window just downstream of the fuel injection zone and a circular window on the top of the rig's downstream end near the scramjet exit. Visualization and video recording of both windows was made possible by affixing a mirror over the top port to reflect the image towards the camera.

A series of still frames from the video recording of Test 1 are shown in Figures 13. These are arranged in time sequence in accordance with the test operating sequence as summarized in Table IV. The video recorders were turned on after the pre-heater operation was stable and just prior to scramjet light off on ethylene. That was approximate thirteen second period from the time of pre-heater ignition. The top grouping of Figure 13 is from the video recording of the test bay side view camera. In this view, the scramjet side window view port and the mirror reflection of the scramjet exit top view port can both be seen. The lower grouping of Figure 13 is from camera recording of the top view port directly.

Table IV
Scramjet MHD Demo Test Operating Sequence

<u>Action</u>	<u>Approx. Time (sec)</u>
Cooling Water on.....	0
Air On	0
- Torch Light-off	0
- Heater H ₂ /O ₂ to Set Conditions	5 - 7
- Scramjet C ₂ H ₄ Fuel On	8 - 9
NaK Seed Flow On	10 - 11
MHD Test	11 - 14
NaK Seed Flow Off	15 - 16
- C ₂ H ₄ Fuel Off	15 - 17
NaK Argon Purge On	17 - 22
Cooling Air On	22 - 600
Continue Low NaK Argon Purge ...	22 - 600

TABLE V
SUMMARY OF SCRAMJET MHD POWER DEMO TESTS

Test No (UTRC)	Test Date	Load Dump Setting (Ohms)	Magnet Current (Amps)	Peak Magnetic Field (Tesla)	Test Duration (Sec)	Comments
1 (213.1)	12/11/2006	8.20	70	1.48	30	Nominal Operation Observed
2 (213.2)	12/11/2006	27.20	70	1.48	26	Nominal Operation Observed
3 (213.3)	12/11/2006	1.95	70	1.48	24	Nominal Operation Observed
4 (214.2)	12/12/2006	11.00	85	1.80	30.00	Anomalous Scramjet Pressure Distribution Observed
5 (214.3)	12/12/2006	11.00	85	1.80	28.00	Repeat of Previous Test Condition Nominal Operation Observed
6 (214.4)	12/12/2006	7.25	85	1.80	23.00	Nominal Operation Observed
7 (214.5)	12/12/2006	32.75	85	1.80	22.00	Nominal Operation Observed

Note: UTRC test 214.1 was attempted but a premature, controlled shutdown occurred due to scramjet wall thermocouple over-temperature trip out.

The luminance and hue of the combustion flame from the view ports as sequenced in time is consistent with the various stages of test operations. The bluish glow seen in the side view camera when the scramjet was ignited is seen to intensify in brightness as the scramjet ethylene fuel flow was ramped up to its final setting (Figure 13, 14.93 sec to 23.47 sec). In the top view port during this same general time period, the luminance is seen to change from bright white to a reddish hue. This is color change as the scramjet is brought up to full flow condition is a result of the bottom steel heat sink wall of the scramjet exit heating up and starting to glow red.

The extremely bright luminance and purplish hue color that is occurs with NaK injection is characteristic of alkali metal flames and provides evidence of seed in the combustng flow and an accompanying expectation of plasma generation. Initiation of the MHD power generation period is consistent with turn-on of the seed flow.

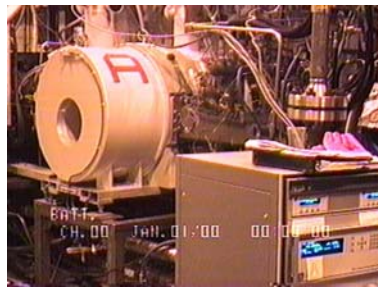
It is interesting to observe that the purplish hue to the flame persists in both view ports after the NaK flow was shutdown with the scramjet combustor still in operation (fifth sequential frame shown in the figures). This observation is evidence that residue NaK existed in the system, most likely deposited on the walls of the pre-heater. This residue is being drafted with the in-coming air flow providing some low concentration of alkali metal vapor giving rise to the sustained purplish hue.

The test shown in Figures 13 was the first firing of the MHD demonstration test series. In this test, the test train was clean prior to operation. In subsequent tests, evidence of NaK residue in the scramjet rig was also seen in the MHD electrical measurements. A slight amount of electric power generation occurred with scramjet light-off (prior to seed injection). In general, this is hypothesized to be due to a low concentration of seed in the stream from pre-existing residue deposits, providing for a slight ionization to the scramjet combustion exhaust.

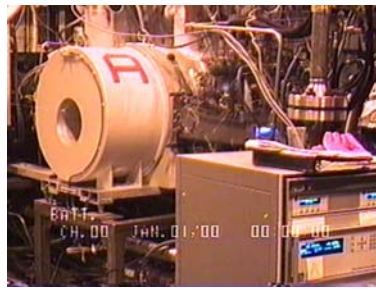
IV. POST-TEST DATA AND ANALYSES

A. Scramjet Engine Data Evaluation

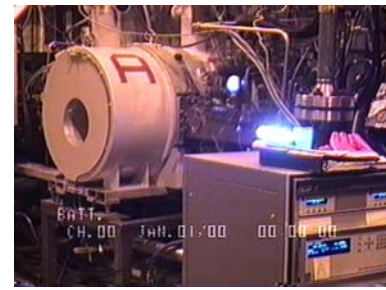
The first effort in post-test analysis of the test results was that of verifying the scramjet combustion process. This was accomplished by UTRC following the same basic data evaluation procedures used in their scramjet development research with the existing test rig. Scramjet data evaluations included reduction of the calorimeter data from each test to estimate the heat release and provide an approximation of combustion efficiency. It is noted that calorimeter data is subject uncertainty based on the nature of the measurement; however, for the existing system there is a good degree of confidence in this measurement based on the past test history and data base that exists.



Pre-Heater Light (13.00 s)



Scramjet Ignition (14.93 s)



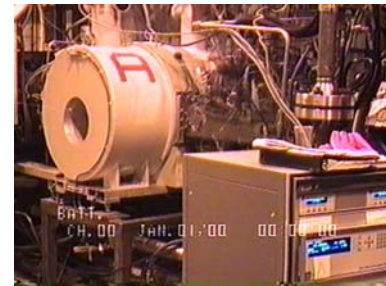
Scramjet Stable (22.47 s)



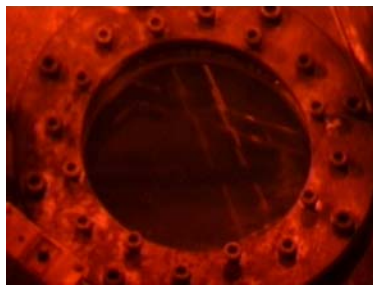
NaK Injection On (22.67 s)



NaK Injection Off – Engine Lit (26.13 s)



Shutdown – Purge Cooling (26.82 s)



Pre-Heater Light (13.00 s)



Scramjet Ignition (15.22 s)



Scramjet Stable (22.31 sec)



NaK Injection On (22.55 s)



NaK Injection Off – Engine Lit (26.01 s)



Last Recorded Frame (27.80 s)

Figure 13. Photographic Sequence of Test No. 1

The second effort in the scramjet combustion analysis was to plot and assess the distribution of wall pressure data along the length of the scramjet test article. These data also have a large established data base from previous experiments and also from CFD analytical verification. The static pressure distribution data in comparison to CFD results and past tests, provides a high degree of confidence that operation of the scramjet was normal.

Figure 14 presents the UTRC data analysis of the calorimeter data inferred demonstrated combustion efficiency. These combustion efficiency estimates were derived by comparing the calorimeter data from each test to computed equilibrium combustion without consideration of the presence of NaK. The effect of NaK on the combustion process was subsequently evaluated by LyTec and revealed a slight elevation of heater total temperature and a slight decrease in the scramjet flame temperature.

Bar graph presentations of the seven MHD test points are shown in comparison to the Mach 8 baseline test results that were obtained in March 2006 without the MHD test train in place. The tests ran on the first day of MHD testing showed combustion efficiencies levels that were consistent with that past result (80% to 90% nominal). Contrary to this, the tests ran on the second day of MHD testing were determined to be noticeably lower in implied combustion efficiency than nominal (75% to 82.5% mean).

The other characteristic of the reduced calorimeter data derived combustion efficiency estimates is the large error bar that is associated with each measurement. The accuracy of these results is considered to be within ± 7.5 of the mean value; primarily due to lack of a sustained, steady state flow and burning conditions. Moreover, scramjet combustion tends to be unsteady and cyclic in nature due to development and shedding of vortices in the burning zone and the presence of movement the shock train.

UTRC evaluated scramjet static pressure distributions for the seven MHD power tests are shown in Figure 15. The seven MHD tests are plotted as distributed symbols over a background trace which was taken from the Mach 8 baseline test ran in March 2006 without the MHD test train in place. The period of the test in which these data were extracted for evaluation was during the MHD power generating period.

The overall observation made from the static pressure data is that these data near identical to those from the baseline test. The noticeable exception to this is Run 4 in which an anomalous distribution is apparent. It is hypothesized that in Run 4 the shock train moved back ahead of the scramjet forcing the rapid static pressure increase in front of the combustion zone.

The scramjet static pressure data distributions for the first series of MHD powered tests (Day 1) followed that seen in the baseline test with a slight elevated static pressure exiting the scramjet. This behavior is consistent with the observed higher combustion efficiency exhibited by the first test series. The static pressure data distributions for the second series of MHD powered tests also followed reasonably well the baseline test data with near agreement in the exit static pressure level.

Based on UTRC's assessment of these pressure distribution traces as well as the inferred combustor efficiency evaluations, it was concluded that the presence of the operational MHD generator downstream of the scramjet produced "little to no effect" on normal operation and performance of the scramjet. This determination was one of the major elements of the test results that was sought by the HVEPS research team.

B. MHD Generator Electrical Data

A summary of the MHD power demonstration test set points that were conducted in two test series was provided in Table V. In all of these tests, electrical output data from the generator was successfully recorded with the UTRC dedicated DACQ Model 370EN acquisition system. This system collected eight channels of generator electrical data at a rate of 1kHz each. MHD generator global output can be derived by summation of the ΔV 's across the generator length (upstream to downstream power take-off connections).

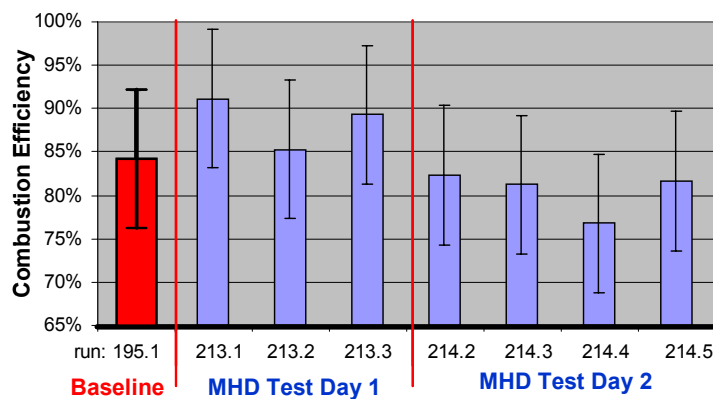


Figure 14. Scramjet Combustion Efficiency Evaluations from Calorimetry Data for MHD Power Tests

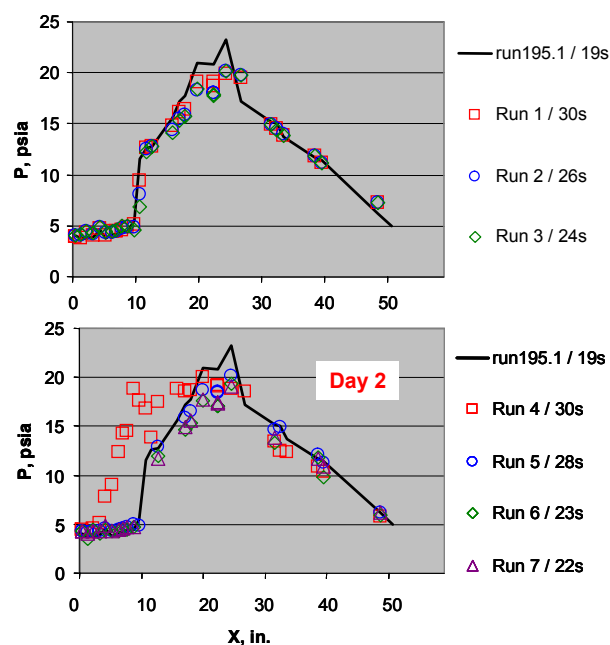


Figure 15. Scramjet Static Pressure Distributions

Typical raw data traces of the electrical output are illustrated in Figure 16. These data traces are for MHD Test No. 1 and show the global voltage across the generator (or load dump) and the net output current. The time period in the data traces covers the MHD power generation period of the test. In Figure 16, seed injection occurs at approximately the 27.68 second time point on the abscissa scale. This can be identified by the sharp rise in the electrical data traces; seen crisp in the current trace. The power generation portion of this test covered approximately 3.0 seconds and is seen in the traces to end at around 30.7 seconds where the current and voltage drop off.

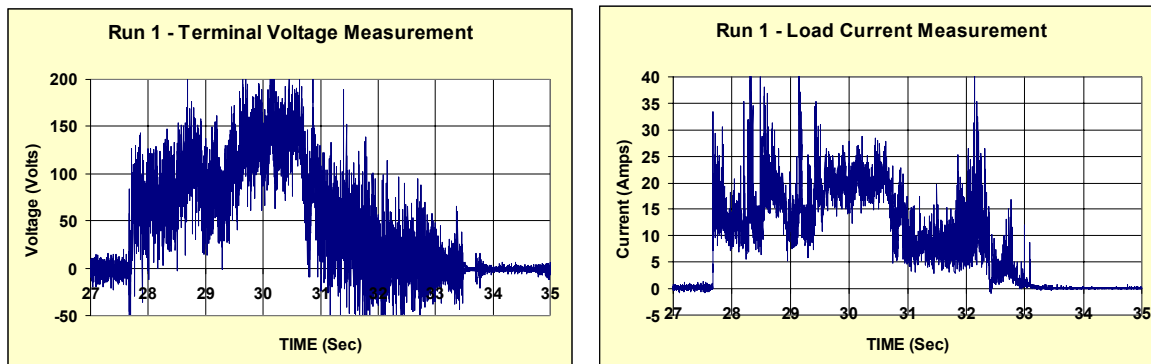


Figure 16. Raw Data of Terminal Voltage and Current (1kHz Data Rate)

Due to NaK residue deposits in the pre-heater, the MHD generator continued to produce power (seen as degrading with time) after the NaK flow was terminated. The spike in the current trace that occurs at approximately the 32.2 second time point is caused by purging of the NaK feed lines. NaK feed line purge was instituted simultaneously with scramjet shutdown. Due to the slower response of the large shutoff valve of the ethylene flow, a very brief period followed where substantial seed was injected while the scramjet is still burning; giving rise to a second pulse of electric power production.

Some characteristics of the raw electrical data traces that deserve mentioning are the instability in the traces and the gradual rise in power that occurs with time during the MHD test period. There can be distinguished two types of fluctuations in the data; one low frequency fluctuation which is a reflection of combustion unsteadiness, and, a very high frequency fluctuation superimposed on the lower one. The high frequency fluctuations are typical of MHD electrical output signals and are driven by arcing in the generator channel (i.e., arcing between the core plasma and electrode wall – across the low impedance boundary layer).

The gradual rise in power seen in the traces during the MHD period is a manifestation of heating of the electrode walls. As the walls become hotter, the boundary layer impedance becomes less and the near wall voltage drop decreases, giving rise to an improvement in net power output.

Digital filtering of the raw data was required in order to obtain traces that were amenable for analyses. In the work that follows, this was accomplished using a ten point time running average. Typical examples of the filtered signals obtained in this fashion for the same data set (MHD Test No. 1) are shown in Figure 17. These filtered traces provide a much clearer view of output signals by averaging out the high frequency components of the signals.

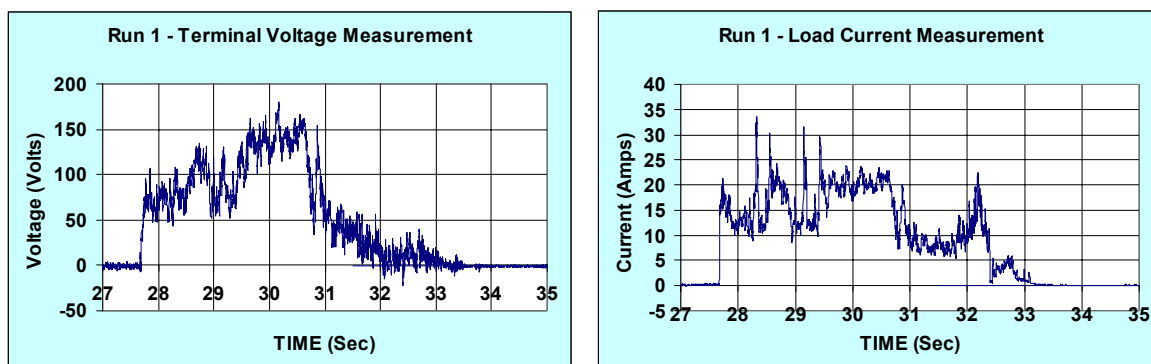


Figure 17. Filtered Electrical Data Used in Analyses – Ten Point Time Running Average

In addition to the UTRC high speed data system, a backup terminal voltage measurement was taken by LyTec using a recordable Fluke multi-meter. The Fluke meter was set to automatically trip (turn on) upon the presence of a threshold voltage level. The recording rate of this device was 50 Hz. The Fluke recordings were downloaded to an analyses PC after each test to provide a quick look at the test results so that a decision could be made on the performance level and where to re-set the load dump resistance for the next test.

In the MHD generator performance analyses that were concluded in post-test data evaluation, the maximum power region on the power traces for each MHD test was selected for examination. In this region, 100 points from the filtered 1 kHz data were taken and averaged to produce single values for the current and voltage differentials that could be used for comparison to theory. The analyst's selection of a region for analyses was subjective and an example is shown in the power traces of Figure 18 by the small circled region.

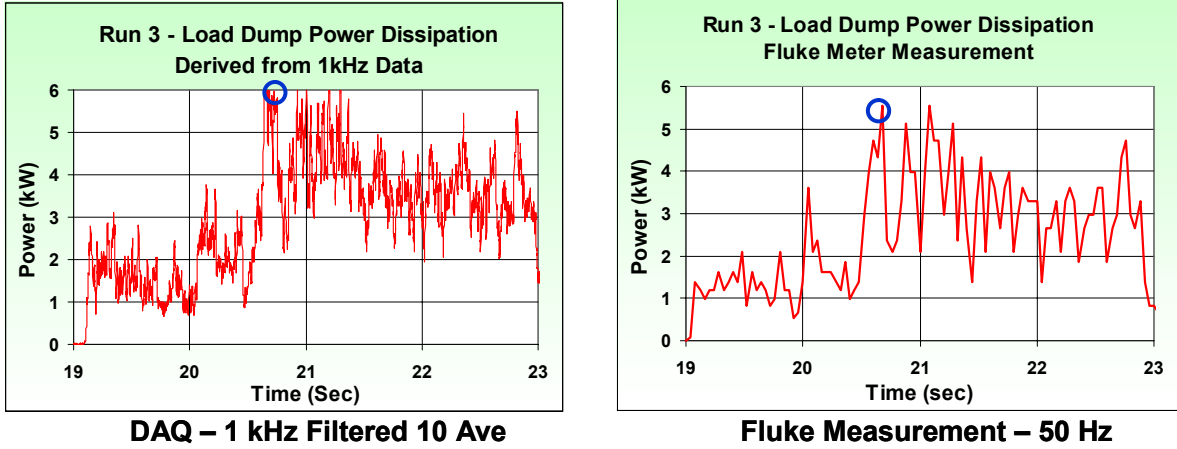


Figure 18. Comparison of Fluke Power Data to Filter DAQ Power Data

MHD generator Hall voltage distributions for the tests are plotted in Figure 19. (Data from Test No 4 in Test Series 2 was not reduced for analysis because of the anomalous scramjet pressure data as discussed previously.) There are two characteristics in the voltage distributions that gauge performance. The first is the slope of the distributions across the length of the plots. The slope of the axial voltage distribution is in fact the Hall electric field (E_x) which is seen to be fairly uniform in the central portion of the channel. The magnitude of the Hall field is inversely proportional to the magnitude of the resistive load across the generator terminals.

The second characteristic of these plots which is most important in evaluating the MHD generator performance is the turn down in the voltage that occurs in the end regions. This turn down reduces the terminal voltage across the load dump (such as measured with the Fluke meter). It is also not a true reflection of the actual MHD generator electric output. The turn down of voltage in the end regions is caused by a reversal of the Hall field in the power take off (PTO) region. As illustrated in Figure 20, this reversal causes an abrupt reduction in voltage level which degrades terminal output voltage.

To explain the electric field reversal phenomenon, consider Equation 5 which is an algebraic expression for the local Hall electric field,

$$E_x = \frac{(G + \langle \beta \rangle^2) I_{Load} - \langle \sigma \rangle A_x \langle u B \rangle (1 - \Delta) (\langle \beta \rangle - \Phi)}{\langle \sigma \rangle A_x (G + \Phi^2)} \quad (5)$$

where the bracket terms (i.e., $\langle \rangle$) represent integrated average values of the contained properties/quantities over the local cross-plane of the generator flow stream. The various terms/parameters in Equation 5 are standard in diagonal MHD theory; G is Rosa G -factor (Eq. 3), σ is plasma electrical conductivity, β is Hall parameter, σ is conductivity, uB is the induced EMF, Δ is the near electrode voltage drop factor¹⁵, Φ is the $\tan \theta_w$ (θ_w is the physical diagonalization angle with $\tan \theta_w = E_y/E_x$), and A_x is vertical flow cross-sectional area.

In Equation 5, I_{Load} is the electric current through the terminal load dump and is conserved throughout the active part of the MHD generator channel. Under the power generation mode operation of an MHD generator the Hall electric field

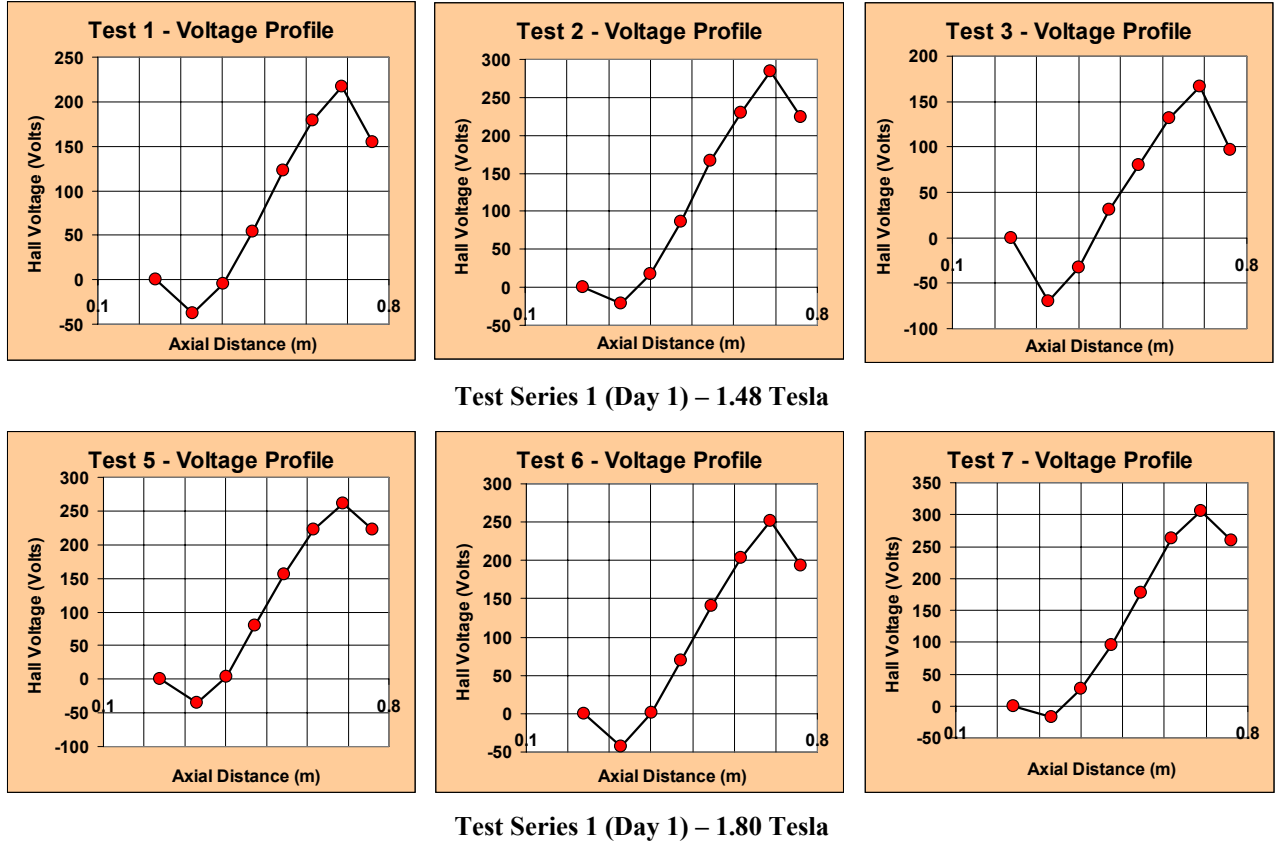


Figure 19. Measured MHD Channel Voltage Distributions

is negative. By setting the Hall field equal to zero (where the sign of the Hall field reverses) and solving for I_{Load} , the following results,

$$@ E_x = 0, \quad I_{Load} = \frac{< \sigma > A_x < u B > (1 - \Delta) (< \beta > - \Phi)}{(G + < \beta >^2)} = I_{sc}(x) . \quad (6)$$

The functional expression in Equation 6 is the local short circuit current, $I_{sc}(x)$, in the plasma and represents the maximum amount of current the generator can produce at any axial location. When the generator load current exceeds the local short circuit current, the Hall field will reverse direction leading to a reduction in the Hall voltage, i.e.,

when; $I_{Load} < I_{sc}(x)$, then $E_x < 0$, and ΔV is positive (normal generator operation);

when; $I_{Load} > I_{sc}(x)$, then $E_x > 0$, and ΔV is negative.

As seen in Equation 6, $I_{sc}(x)$ is directional proportional to the local intensity of the magnetic field, $B(x)$. When the magnetic field distribution decays severely in the end regions of the MHD generator channel (e.g., PTO regions), then Hall field reversal can occur. This was the case for the MHD demonstration tests as evidenced by the strongly decaying magnetic field distribution shown in Figure 5.

What phenomenologically occurs in the end regions when Hall field reversal occurs is that a portion of the electric power generated by the active “central” part of the MHD generator is being deposited back into the plasma. If reversal is strong enough, then the Faraday current density, J_y can also reverse direction – reversing the direction of the

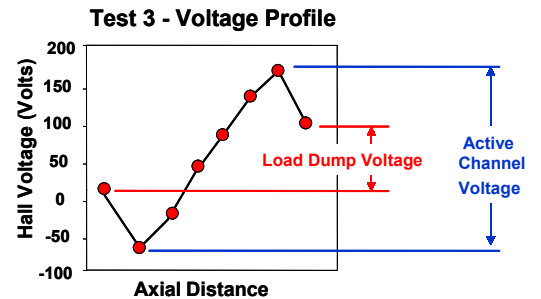


Figure 20. Illustration of End Effect – Hall Field Reversal

Lorentz body force and leading to the end regions actually operating in the MHD accelerator mode and providing acceleration to the plasma stream.

To avoid the presence of power losses in the PTO regions of an MHD generator requires the use of current controls on the PTO electrodes. The controls can be active using power electronics or passive using a resistive network. In such a control circuit, the load current is controlled to decrease across the end region such that its local level never exceeds the local short circuit current.

No active PTO current controls were used in the HVEPS MHD demonstration testing due to limited resources for additional diagnostics and also due to the general nature of the focused test power demonstration objective. Consequently, some end region Hall electric field reversal was anticipated but the degree of this as seen in the final voltage distribution data was large, approximately 25% to 60%. This load dump power production is not considered to be a true reflection of the power production capability of the demonstration test MHD generator since the end loss are controllable. With that theme in mind, post test analysis concentrated on validation of the central portion of the MHD generator as the true measure of performance. Moreover, validation of the Hall electrical field and MHD power density in the central region.

Presentations of the MHD generator electrical output for the tests of each test series are shown in Figure 21. The data points therein were taken from data screening (as discussed above) and the time period selected for presentation was a high output period for each test. The test data points in Figure 21 are plotted on the pre-test performance maps used in actual test operations. It is noted that these pre-test maps were constructed for peak magnetic field intensities of 1.5 and 2.0 Tesla. Whereas, in the actual tests the peak magnetic field were estimated at 1.48 and 1.8 Tesla for MHD Demo Test series 1 and 2, respectively. It is also noted that the pre-test performance maps were generated for a projected combustion efficiency of 85%, whereas, the combustion efficiency of the actual test points varied considerably (see Figure 14).

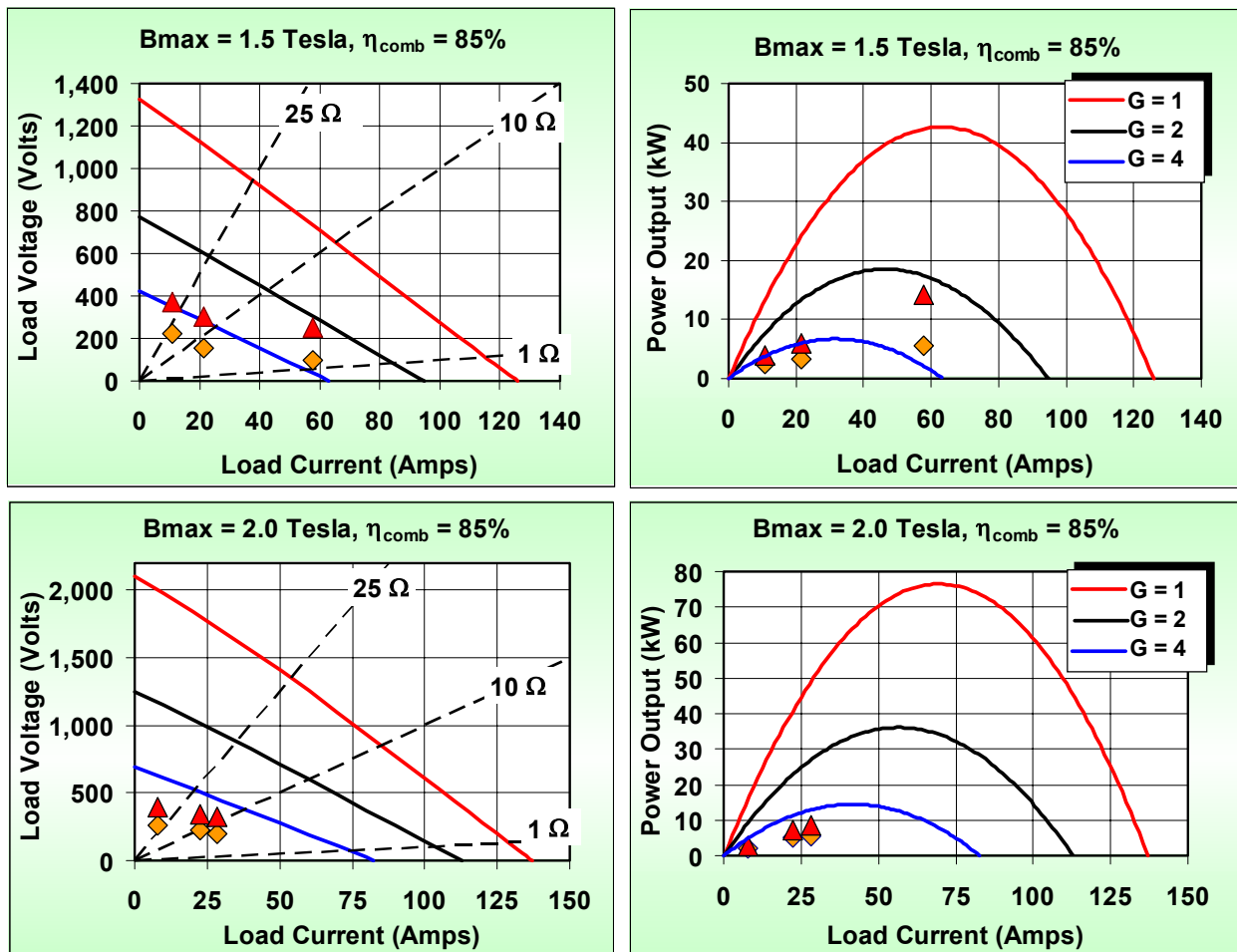


Figure 21. HVEPS MHD Demo Tests Global Electrical Output in Comparison to Pre-Test MHD Performance Maps

Two different symbol data points are shown in Figure 21 for each individual test. The lower value point represents the electrical output as measured at the load dump. The upper point represents the electrical output for each test with the Hall field reversal end effect removed. The upper point is the more viable measurement of the electrical performance of the active portion of the MHD generator, an indication of the real potential difference generated. This active portion point was derived from post-test analysis.

The MHD power demonstration data points for the first test series runs as plotted in Figure 21 show performance levels in the range that was anticipated runs at the lower peak B-Field. Those for the second test series are lower than anticipated. However, the pre-test map for these data is was constructed for a 2.0 Tesla peak field and a combustor efficiency of 85%. The actual second series of tests were conducted at a peak B-field of 1.8 Tesla and the demonstration combustion efficiency level for second series was between approximately 75% and 82.5%

C. MHD Generator Post-Test Performance Analyses

The MHD generator performance was evaluated utilizing LyTec's MHD generator design and analysis computer code. This code has been used in the past to analyze and validate a myriad of MHD power test results for both small scale and large scale experiments.¹⁶⁻¹⁷ In terms of the methods content, the generator code is quasi-2D in nature with one dimensional plasmadynamics coupled to two-dimensional electrodynamics. It is further noted, that the same code used in the following analyses was also used to design the generator channel for the HVEP scramjet MHD demonstration tests.

The basic LyTec generator code solves the governing conservation equations with inclusion of viscous terms and heat transfer. It employs a boundary layer model to incorporate boundary layer effects for both the plasmadynamics and also for evaluation of near electrode electrical losses. The electrodynamics solves the generalized form of Ohm's law, cast into solution for the diagonal loading configuration, to define the Faraday and Hall components of the electric field and current density, i.e., E_y , E_x , J_y , J_x , respectively). Provisions are included in the code through empirical models to simulate near electrode arcing and inter-electrode current leakage effects. The electrodynamics equations directly incorporates the effect of plasma non-uniformity through use of the Rosa G-factor (G , see Eq. 3) as a parameter in the governing equations. In addition, Wu Δ -factor¹⁵ (Δ) is also used to account for the effect of near wall voltage drop outside of that attributable to G .

The code can be run in either the design mode or analysis mode. In the design mode, a desired thermodynamic distribution can be imposed and the code can be run to define the generator loft and optimum loading. In the analysis mode, the code physical geometry is specified and solution is obtained for a fixed loading condition. Special algorithms are available in the code to enforce operation at maximum power or a Hall current neutralized condition. These algorithms can be employed in design phase of an MHD generator to define loading optimization. Similarly, the code also has algorithms to facilitate the design of the power take-off circuitry for current control in the end regions to mitigate Hall field reversal losses.

It was hypothesized that three factors would enter into the MHD power demonstration test that would need to be reviewed and quantified in the MHD generator electrical performance analysis efforts. These three factors are as follows:

- 1) *Seeding Efficiency* – Providing an effective NaK seeding scheme to allow for sufficient time and mixing to occur for the NaK to evaporate, dissociate and ionize (i.e., maximize ionization fraction) to produce a quality plasma entering the MHD generator channel to promote the MHD power process;
- 2) *Combustion Efficiency* – Achieving as high a scramjet combustion efficiency (heat release) as possible, to maximize the bulk plasma temperature and achieve the level of electrical conductivity in the thermal plasma needed to promote the MHD power process;
- 3) *Plasma Non-uniformity* - Achieving as uniform a flow structure as possible to the flow exiting the scramjet to minimize MHD power losses associated with non-uniform plasmas.

The first two of these items should be obvious to the reader. Both *Seeding Efficiency* and *Combustion Efficiency* promote plasma scalar electrical conductivity in a combustion (thermally ionized) plasma which is directly proportional to MHD power density. The third item, *Plasma Non-uniformity*, may not be as obvious to the inexperienced reader. Plasma non-uniformity reduces the bulk plasma conductivity (general plasma conductance) which in turn reduces MHD power density. Plasma non-uniformity effect is mathematically contained in the level of Rosa G-factor and is inversely proportional to MHD power output.

Outside of maximizing burn out efficiency, the UTRC scramjet test article was not designed with the other two items as design criteria. Consequently, the degree to which these items would effect MHD performance were unknown prior to conduct of the HVEPS scramjet MHD power demonstration test. It was contended by the GA team that placement of the NaK seed injector in the head flange of the pre-heater would minimize any MHD performance loss caused by poor seed ionization. The seeding configuration that was used, pre-mixed the NaK seed spray with the incoming H_2 - O_2 heated air over a lateral mixing length of 24 inches. This mixture was drafted through the small flow area test rig's choked nozzle

(1/2 inch x 6 inch throat passage) prior to acceleration to the scramjet combustion zone. It is contended that this approach assured a well mixed NaK concentration in the incoming air stream. The only unknown element related to evaluation of the performance of the seeding is an exacting flow rate in each tests. The seed injection system was pre-calibrated to produce the desired seed flow rate over the pressure differential of its driving pressure and the pre-heater back pressure on the injector. No direct measurement of this flow rate was made during the testing. It is plausible that residue NaK may have settled on the injector tube walls and to some degree affected (reduced) the seeding rate with time.

In any case, in the analysis of the MHD generator test results, no attempt was made to quantify the possible effect of an anomalous seed flow rate (seeding percentage) on power performance. Similarly, no attempt has been made to quantify the possible effect of reduced ionization fraction. The plasma quality utilized in these analyses was considered to be a partially ionized thermal plasma as computed using LyTec thermochemical equilibrium combustion code which computes the plasma electrophysical properties.

The post-test MHD performance analyses were structured to evaluate and quantify the effects on power performance due to the degree/level of combustion efficiency and plasma non-uniformity as inferred by the experimental data. In addition to this, it was also extended to provide a definition of the potential maximum electric power plausible in each test if a precise load matching would have been used.

The MHD generator performance analyses began with construction of a thermodynamic/electrophysical property file which was used in all data analysis studies. The thermo plasma file was computed using LyTec's thermochemical equilibrium combustion code (with electrophysical properties) with input of the set flow rates of all combustion reactants (O_2 , H_2 , NaK/argon, ethylene, and air). These flow rates are defined in Table IV. An adiabatic combustion process was computed to define the base thermo plasma file. The thermo plasma file was written into a lookup table with gas dynamic and electrophysical properties tabulated against pressure and temperature. In the generator modeling, the code interpolates off this table to provide a solution to the equation of state for this real gas mixture.

LyTec's combustion thermochemical equilibrium code does not have the capability of computing unreacted species (unburned fuel), whereas, UTRC's rascal code can. Since unreacted species is the measure for combustion efficiency, UTRC's code was run for variable combustion efficiency to provide a map of the scramjet inlet thermodynamic state as a function of burnout. LyTec utilized UTRC's results to define the MHD generator entrance bulk thermodynamic state as a function of combustion efficiency imposing a heat loss on the base thermo plasma file to define the MHD generator entrance conditions consistent with UTRC's predictions.

Figure 22 shows plots of LyTec's MHD generator entrance state variation with combustion efficiency. Also contained on Figure 22 is a tabulation of the UTRC derived combustion efficiencies for each test of the MHD power demonstration test series.

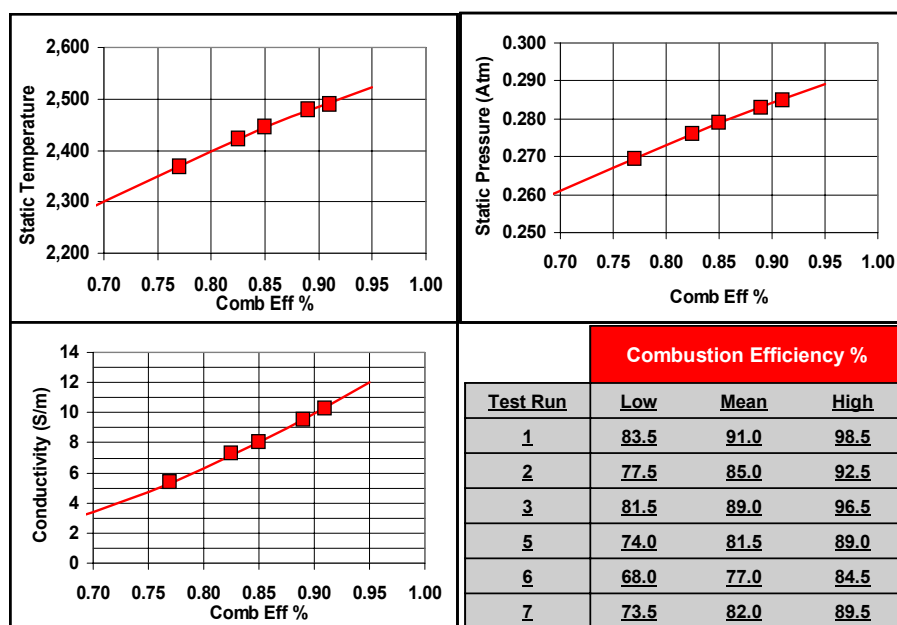


Figure 22. MHD Generator Channel Entrance Thermodynamic State as Function of η_{comb}

With the thermo plasma file preprocessing completed, the MHD generator data evaluations preceded along two paths. In one path, the nominal combustor efficiency for each of the six tests analyzed was fixed in accordance with UTRC's estimates and a unique set of MHD channel entrance conditions was determined for each test. All other computer code inputs related to geometric specifications, magnetic field distribution, PTO current control, and factors affecting wall losses (shear and heat transfer) were similarly set a fixed values.

Heat transfer is controlled by wall surface roughness and a specified wall temperature. Since the HVEPS demonstration test utilized a heat sink copper MHD generator channel the actual wall surface temperature is time variant. For analysis purposes, a hot wall condition of 1,000K was imposed on the calculations. This wall temperature value produced a generator inlet heat flux level that was consistent with UTRC's estimate and consistent with the analyst's experience for similar MHD systems.

In imposing current control over the PTO end regions of the generator channel, the codes algorithm was imposed to force the generator load current along the generator short circuit current distribution across the three PTO electrodes on each end. In this fashion, the computed performance does not suffer from the large end effects power losses caused by Hall electric field reversal.

The next exercise in the analysis was to run a series of MHD generator calculations with perturbation of G-factor. This exercise concluded when the G-factor value was found for which the computed central Hall voltage distribution showed a near match to the experimental data. The G-factor evaluation was accomplished for all six tests and the variation in G between tests was logged.

The final step in the MHD generator analysis was to determine what level of maximum power could have been produced in each individual test if the external load was matched to the generators internal impedance. To accomplish this, the determined G-factor for matching the measured data set (from the previous step) was held fixed and calculations were performed by variation of the load current from short circuit to open circuit conditions. These calculations were used to construct generator operation loadlines and power maps for each individual test. The maximum power potential for the MHD generator at each individual test specific conditions is determinable as the peak point on the power map trace.

The second path in the analyses effort proceeded identically as described above with the exception that the combustion efficiency for each test was fixed at the low and high values. This provided bounding of the MHD performance and inferred G-factor as a function of combustion efficiency

4.5.2 MHD Performance Analysis Results

Presented in Figure 23 are the summary results from the model to data comparisons derived from computing model to data matches for each MHD demonstration test when subject to the nominal efficiency value. The results show plotted central region Hall voltage data in comparison to computed Hall voltage distribution from the MHD generator model. The agreement between data and theory is considered good in both the slope of the voltage distribution (level of E_x) and the magnitude. This is evident in all data sets and consistent across the entire distributions. Some decay in voltage in the end regions is seen in those tests that were conducted at higher load currents and this is considered a real effect since the PTO region was short in length.

The value of G-factor required to achieve the model to data matches of Figure 23 is noted in the title of the plots. The test which produced the highest power output (Test No. 3) was that test which exhibited the lowest G-factor. The end-to-end level of Hall voltage seen in the Test Series 2 data is lower than one would expect with the higher peak B-field setting. This leads to the conclusion that the differentiation between performance of the Test Series 1 and Test Series 2 is mostly influenced by the reduced combustion efficiency experienced in Series 2.

Representative plots of the computed plasmadynamic and electrodynamic distributions along the MHD generator flow path are shown in Figures 24 and 25, respectively. The distributions include the flow through the transition duct and diffuser. These distributions were taken from the results of the model to data matching analysis for Test No. 3.

The final results of the analyses of each test point at their nominal combustion efficiencies with fixed code inputs and perturbation in G-factor to achieve a model to data match are shown in Figure 26. Therein is presented the computed MHD generator performance maps for test conditions consistent with those of each individual test point. In general, operational loadlines and power maps were constructed for each individual test point. Test results are plotted as single symbols with the lower symbol being load measured conditions and the upper point being results of analysis neglecting the power loss due to the PTO end effects (Hall field reversal). It is noted that each line in Figure 26 passes directly through the upper data point for the test associated with that line (note color coding).

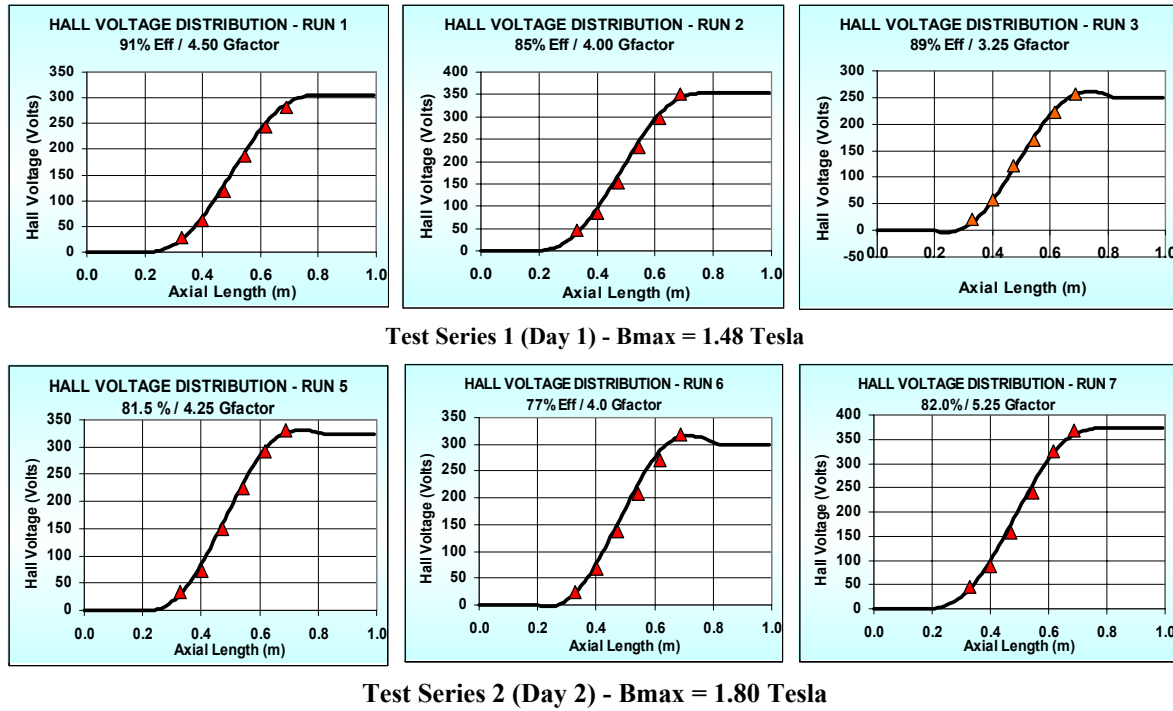


Figure 23. Results of Model to Data MHD Performance Analyses for Demonstration Test Points at Nominal Combustor Efficiency Values

In Figure 26, the maximum power point on the elliptical power map individual lines is a prediction of the maximum electrical power that could have been generated in that specific test if the external resistive load was matched to the overall generator internal impedance. In most cases, the actual load setting was towards the open circuit side of the operational loadline. However, Test No. 3 (at 1.48 Tesla peak B-field) and Test No. 6 (at 1.8 Tesla peak B-field) were set very close the maximum power generating conditions.

The disparity in the level of MHD power generation between the low and high B-field settings is notable. For example, Test No. 3 produced nearly twice as much electric power as Test No. 6. For the exact same scramjet operating conditions, it would anticipated that Test No. 6 would be on the order of 1.5 times higher than Test No. 3 (i.e., $P_d \sim B^2$).

In assessment of the maps in Figure 26, it is observed that the short circuit current (location where loadline intersects the abscissa) for the high B-field tests is generally lower than that in the low B-field tests. This observation is an indication that the electrical conductivity, σ , in the high B-field tests was reduced from that experienced the previous day (i.e., $I_{sc} \sim \sigma$).

The open circuit voltage (location where loadline intersects the ordinate) levels for both test series appear in the same general range. Open circuit voltage is directly proportional to induced EMF, $\langle uB \rangle$, and inversely proportional to the G-factor, G . One can conclude from this that a noticeable increase in the open circuit voltage in Test Series 2 over that of Test Series 1 should be apparent. Since this isn't the general case seen in comparing the test series, a suspicion arises as to whether the mean velocity, $\langle u \rangle$, was reduced in Test Series 2.

Results from the second analyses effort are shown in Figure 27. This analyses utilized the bounding combustion efficiencies (upper and lower) for the test points as tabulated on Figure 22 to determine loadlines and power maps for the test points at these extreme combustion efficiency levels. In general, all resulting loadlines and power maps generated for each test point were forced to match the experimental electrical data for each respective point. What this constraints means is if the MHD electrical output is fixed and the combustion efficiency is lowered, the G-factor required to achieve a model to data match will be forced to a lower level. When the combustion efficiency is increased, the opposite must occur.

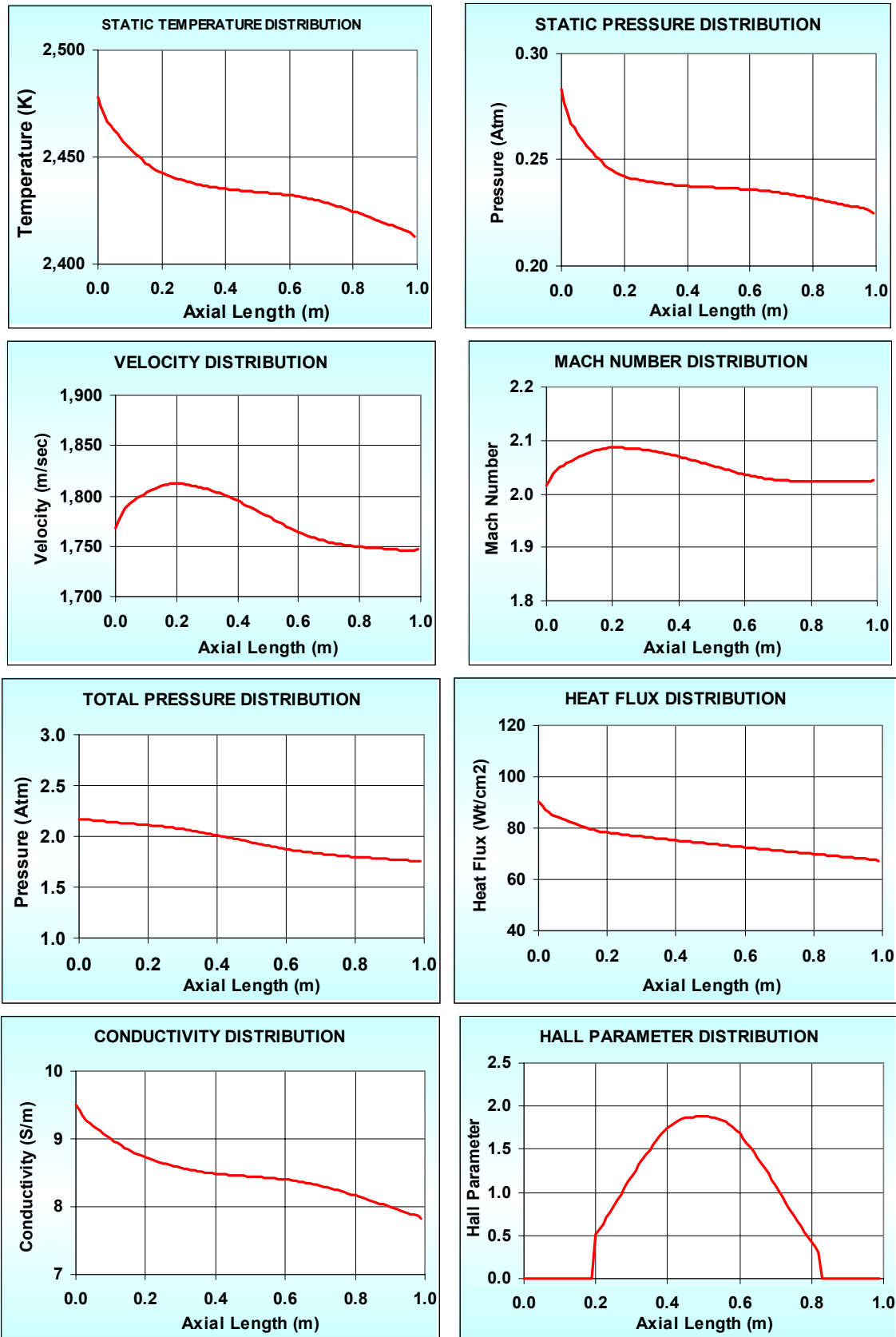


Figure 24. Distributions of Plasmadynamic Properties Along the MHD Generator Flow Train for Test No. 3

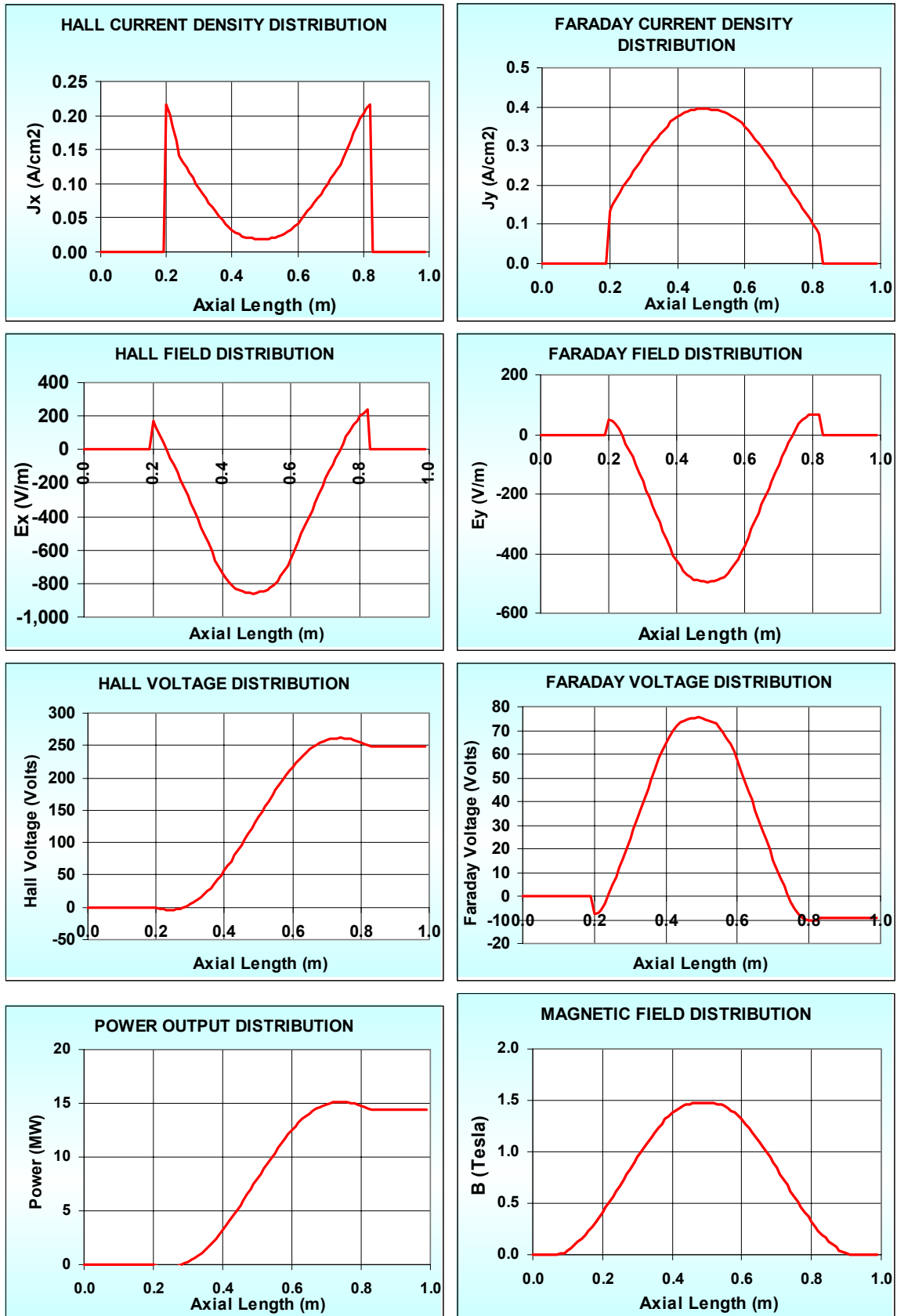


Figure 25. Distributions of Electrodynamics Along the MHD Generator Flow Train for Test No. 3

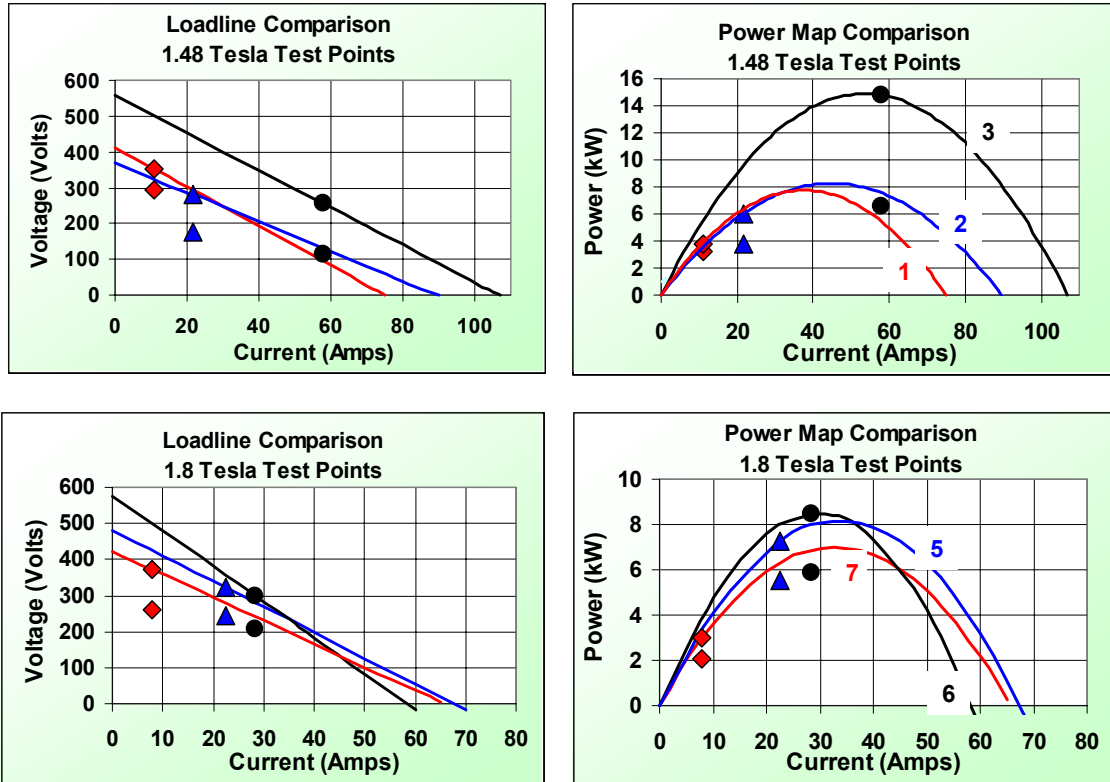


Figure 26. Computed Loadlines and Power Maps for All MHD Demo Test Points with Operation at Nominal η_{comb}

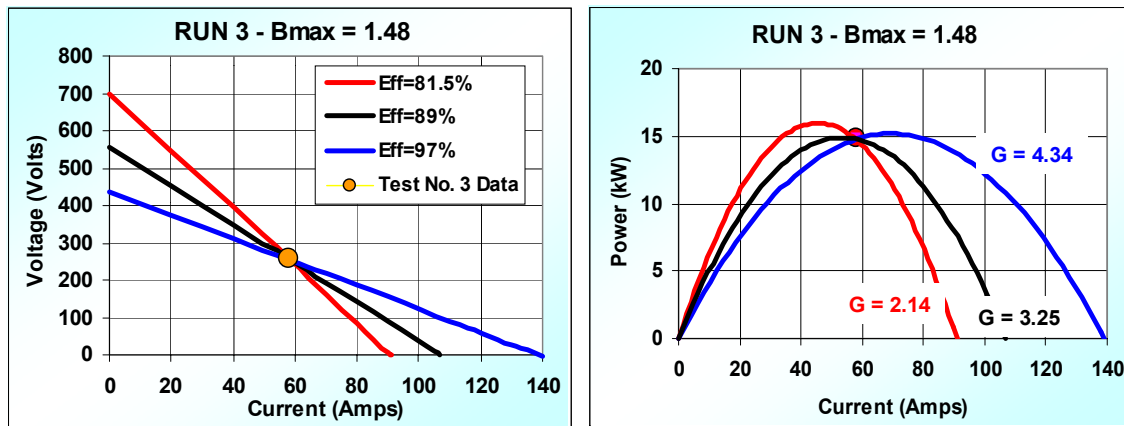


Figure 27. Effect of η_{comb} on Performance – Test No. 3 Model to Data Match at High and Low η_{comb}

The results produce bounding ranges on the loadlines and power maps for each test point. Figure 27 shows this type of result for Test No. 3. It can be seen that the G-factor required for this test varied across its combustion efficiency bounds by a factor of more than two.

Forcing a model to data match as done in Figure 27 requires that the location of the actual fixed data point must shift its position/location on the loadline. A higher combustion efficiency is synonymous with an increased plasma electrical conductivity, σ , which results in a higher short circuit, I_{sc} , terminus point on the loadline. For the loadline to pass through the actual data point, this means that it must rotate towards a lower open circuit voltage terminus point. In order for this to occur in the modeling used, the G-factor must increase. For a lower combustion efficiency, the opposite occurs, i.e., I_{sc} must decrease and G-factor must increase. (There exists situations where this type of match is impossible, i.e., when $I_{sc} < I_{Load}$, or, when G is forced less than 1.0).

The bound power maps resulting at the combustion efficiency bounds exhibit a different level of maximum power point. This is seen in Figure 27. The maximum power for the low efficiency curve is 16 kW; that for the high efficiency curve is 15.2 kW. Whereas, for the nominal efficiency analyzed previously for this point the maximum power was 14.8 kW. In general, very little difference in the potential maximum power production capability is seen. The reason for this is the Test No. 3 load setting was very near a maximum power setting. Test No. 3 exhibited the best MHD performance of the two test series and for that reason it is shown here. Much more discrepancy in power output between the combustion efficiency bounds was seen in the other tests, however, none approached the level of output achieved in Test No. 3.

4.6 MHD Power Demonstration Test Performance Summary

Table VI provides a summary tabulation of the MHD power demonstration test results including both the measurements and the analysis results. For Test No. 3, this table gives results across the η_{comb} bounds as obtained from analysis. The better MHD electrical performance of the demonstration tests was achieved in the first test series where operation was at the lower magnetic field intensity. The reduction in performance in the second test series at the higher field was hypothesized to be due to differences in the effectiveness of the scramjet combustion process and possibly to unidentified operation anomalies. One possible reason for the performance reduction for Test Series 2 could be due to a reduced seeding rate caused by partial plugging of the NaK injector. In order to evaluate this possibility, further extensive analyses on reduced ionization fraction of the plasma would need to be addressed.

A first quantification of the plasma non-uniformity effect on MHD performance for the combustion stream exiting a scramjet was derived from the experiments. This was one of the principal objectives set for the demonstration tests. Inferred levels of Rosa G-factor for the tests fell in the range between 3.25 and 5.25, with a general mean level of around 4.0. This level was in the range anticipated based on pre-test studies.

Figure 28 provides a comparison of the matching G-factors required to match each test data point plotted against combustion efficiency. Each test point's nominal η_{comb} is plotted with the symbols identified and a 5% error bar in efficiency to reflect UTRC's analyses.

TABLE VI
Summary of HVEPS MHD Power Demonstration Test Results

TEST No and Date	Peak Magnetic Field Setting (Tesla)	Load Dump Resistance Setting (Ohms)	Combustion Efficiency ¹ (%)	Current (Amps)	Load Dump Power Dissipation (kW)	MHD Electric Power Output ² (kW)	Maximum MHD Electric Power at Matched Load ³ (kW)	Comment
1 11/12/06	1.48	8.18	91.0	21.55	3.81	6.55	8.24	
2 11/12/06	1.48	27.15	85.0	10.85	3.20	4.00	7.76	
3 11/12/06	1.48	1.95	81.5	57.82	6.52	14.38	15.98	Low η_{comb}
3 11/12/06	1.48	1.95	89.0	57.82	6.52	14.38	14.80	mean η_{comb}
3 11/12/06	1.48	1.95	96.5	57.82	6.52	14.38	15.19	High η_{comb}
5 11/12/06	1.80	10.95	81.5	22.47	5.55	7.25	8.09	
6 11/12/06	1.80	7.25	77.0	28.36	5.83	8.46	8.48	
7 11/12/06	1.80	32.75	82.0	8.00	2.10	2.98	6.94	

Notes: 1. Combustion Efficiency Taken from UTRC Calorimetry Analysis – Accuracy +/- 7.5%
2. MHD Power Generated Across Active Portion of MHD Generator (Neglects End Losses)
3. Maximum Power Potential at Matched Load Condition Derived from Post Test Loadline Analyses

There is no apparent reason why G-factor level should be influenced by magnetic field intensity in a low MHD interaction machine such as this one. It can also be hypothesized that if combustion efficiency was the only “independent” variable influencing the needed level of G , then some sort of common, single correlatable data trend line would occur across the plot field for both series data sets. This type of trend is approximated on Figure 28 by the downward sloping shaded field that is superimposed on the plot. Recall that G and η_{comb} exhibit an inversely proportional relationship when they are applied to force the modeling to match the experimental data (see Fig. 27). However, the most likely physical coupled behavior between G and η_{comb} is that shown by the shaded trend. In reality, increased burnout of reactant species and improved mixing should produce a more uniform exit plasma flow field lending a decrease in the resultant G as η_{comb} increases.

The plot of Figure 28 is a rather tenuous device to use in drawing any definitive conclusions without a much larger data base. However, what can be said related to this figure is that the mean level of G-factor need to match model to data (Test No. 1, 2, 5, and 4) was slightly greater than 4.0. Test No. 3 and Test No. 7 were the exceptions to this statement. Test No. 3 was the best test in terms of MHD performance of all the series tests, Test No. 7 (the last test ran) appeared to be the worst. Extending this observation even further, if one follows the shaded trend to a full 100% efficiency condition, then a projected minimum G-factor of approximately 3.0 is defined.

The MHD performance analyses discussed herein neglected the end power losses caused by Hall field reversal in the power takeoff region. This was the theme since the important measure of performance was the level of Hall electric field and its variation across the active (central) portion of the MHD generator channel. It was noted that the power losses in the end regions were in effect a dissipation of power back into the plasma due to localized reversal of the Hall electric field. From that standpoint, the end regions can affectively be viewed as resistive regions in series with the primary load dump resistance. The level of this effective resistance is quantified for each test point in Figure 29 for assessment.

Figure 29 shows that the equivalent load resistance across the active portion of the MHD generator is the combination of the load dump setting and the equivalent resistance of the end effect. The power dissipation in the two also scales directly with the resistance values. The equivalent resistance of the end regions is seen to be inversely proportional to load current. This is most likely a manifestation of reduced plasma impedance in the end region due to increased joule heat dissipation at the higher currents. In contrast, the power loss in the end region is greater for the lower load current test conditions. This observation points to the contention that the near electrode voltage drop is a strong factor in the end region power loss. No attempt was made in the model to differentiate between the end region voltage drop and the nominal voltage drop throughout the entire generator.

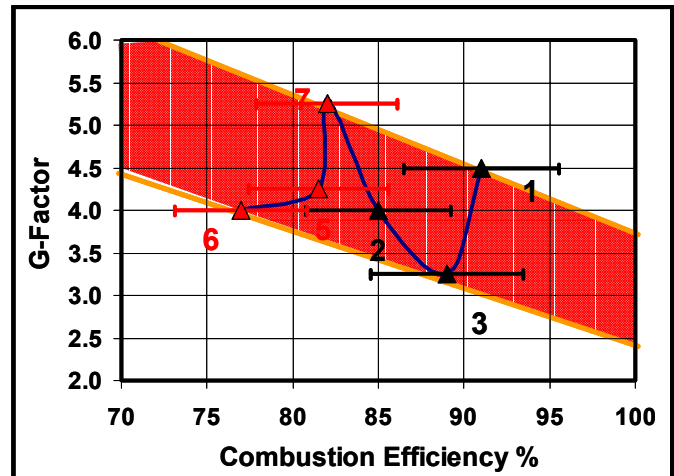


Figure 28. Plot of G-Factor Value versus η_{comb} for MHD Demonstration Test Points as Required to Obtain Model to Data Match

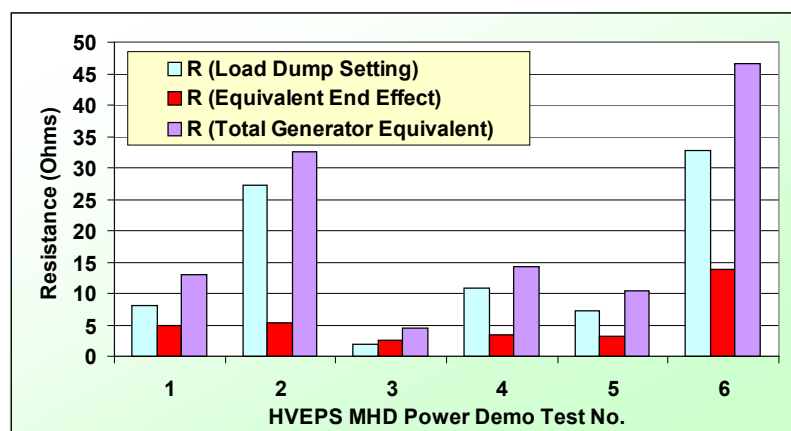


Figure 29. Assessment of Effective Generator Load Resistance

In summary of the phenomenological evaluation of the performance maps generated through analyses; all arguments indicated that a reduction in scramjet combustion performance was experienced in the second day of the MHD power demonstration tests (Test Series 2). This reduced performance was identified as a most likely situation from UTRC's analysis of combustion efficiency (See Fig. 14). However, the real key indication of reduced scramjet performance in Test Series 2 was through actual test observations. The test crew that conducted both series of MHD power demonstration test unanimously concurred that the visual images of each Series 2 test did not seem nearly as brilliant in light intensity as was experienced in Series 1.

IV. CONCLUDING REMARKS

This paper has summarized work concluded under the HVEPS program initiative to research and develop on-board MHD power systems for advanced hypersonic vehicles. The HVEPS program has been active for the past five years and the latest projects under this program are directed at experimental evaluation of airborne MHD power concepts. Two power system concepts are being pursued; self-contained high energy fueled combustion-driven MHD power and scramjet-driven MHD power as integrated in the hypersonic vehicle scramjet propulsion flow path.

Successful completion of the HVEPS scramjet-driven MHD power demonstration tests constitutes a "*world's first*" in showing proof-of-concept of this hypersonic airborne power system concept. It sets the stage for further development of this power system with future work directed at optimization of the coupled system and introduction of continuous duty flightweight hardware. In the longer term, it can be scaled-up and packaged in an integrated, flightweight form for extensive development in a large scale ground test facility or in a flight test.

The goal of future developmental efforts for scramjet driven MHD power generation should initially concentrate on means for improvement in both scramjet combustion efficiency and plasma uniformity. Improvement in combustion efficiency unto itself is probably only marginally achievable. The demonstrated nominal efficiencies of the MHD demonstration tests and other past tests with the UTRC scramjet test article (85% to 95%) is considered quite good for supersonic combustion process over a short length. It is contended that non-uniformity plasma effects can be substantially mitigated with scramjet design changes directed at its optimization. Consequently, improvement in plasma uniformity should be a first priority; possibly by optimization through modifications in fuel injection patterns and other geometric changes. In that context, the goal would be to shift the whole data grouping as seen in Figure 28 downward on the G-factor scale.

Although the MHD performance data analyses efforts of this paper were confined to studies for quantifying G-factor level for each specific data point, this work elusively pointed to the possibility of other factors influencing the overall test results. Three influencing factors that can be identified are briefed in the following bulleted statements

- ✓ Reduced Ionization Fraction. A reduced ionization fraction below that of a thermochemical equilibrium combustion plasma at the preset/design flow rates is a distinct possibility. This could arise from either a lower than targeted seed flowrate (NaK flowrate was not measured) or from ionization ineffectiveness. The ionization process for NaK involves its dispersion into the stream, its dissociation, its vaporization, and then finally ionization of the Na and K atoms. The Na and K ions produced will immediately form neutral hydroxide. It is believed that sufficient flight time existed from NaK injection until scramjet combustion for this process to take place effectively, but there is no absolute certainty that is true.

A reduced ionization fraction will reduce the plasma bulk conductivity and thus reduce overall MHD power performance. No attempt was made in the analyses (thus far) to investigate the effect of a direct plasma conductivity deficit as a parameter. However, the studies concluded on reduced combustion efficiency do reflect that type of results that one would anticipate with a direct plasma conductivity deficit, i.e., a lowering of the G-factor that is required to match the experimental data.

- ✓ Plasmadyamic Wall Losses. No attempt was made in the analyses to perturb the plasmadyamic walls losses to view their effect on MHD performance. The model has the ability to control both wall shear and heat transfer through definitions of surface roughness and wall temperature. All calculations were made for an aerodynamically smooth wall (roughness height of 0.01mm) and at a fixed "hot" wall condition with a wall surface temperature of 1,000K. The wall temperature was set to provide levels of heat transfer at the entrance of the channel in keeping with those provided by UTRC based on measurement of heat flux in the scramjet exit (using thermocouple measurements of temperature gradient within the walls of the steel exit structure).
- ✓ Near Electrode Electrical Losses. Electrical losses (voltage drops) that occur near the electrode walls as current is transferred out of the plasma are known to strongly effect MHD electrical performance. In general, this is confined

to current transport across the cold boundary layers. Boundary layer development leads to the development of extremely high local Faraday electric field in the near wall region; which in most situation leads to arc breakdown discharge from the plasma to the wall. Modeling of near wall discharge effects is an inexact science unto itself since in reality arcs form and then extinguish randomly throughout the generator channel on a extremely short time scale. No attempt was made to perturb the models arcing model to gauge its effect on MHD overall performance. The near wall electrical loss factor (Δ) used by the modeling was set constant for all regions within the generator channel and held constant for all test points analyzed.

Although the three items cited above can have marked effects of computational results, it is not believed that “realistic” parametric studies on these would provide any new insight into the findings of the work as presented herein.

As a final item in summary of the MHD power demonstration testing, it should be noted that the MHD hardware components that were specially designed and fabricated for these experiments performed flawlessly. Upon completing of the MHD demonstration tests and disassembly of the MHD test train, the MHD generator channel was shipped back to LyTec for storage. Overall the channel is still in excellent shape.

ACKNOWLEDGEMENTS

This work has been made possible by resources provided under AFRL Prime Contract No. F22615-01-D02109 to General Atomics under the direction of AF Program Manager Rene Thibodeaux. The authors wish to recognize the entire laboratory technical staff at the UTRC scramjet test facility for their technical and professional excellence in the conduct of the HVEPS scramjet driven MHD power demonstration tests.

REFERENCES

- ¹Lineberry, J. T., Begg, L., Castro, J. H. and Litchford, R. J., “Scramjet Driven MHD Power Demonstration – HVEPS Project Overview,” AIAA-2006-8010, 14th AIAA/AHI International Space Planes and Hypersonic Systems and Technologies Conference, Canberra, Australia, Nov 6-9, 2006.
- ²Lineberry, J. T., Begg, L., Castro, J. H. and Litchford, R. J., “Scramjet Driven MHD Power Demonstration – HVEPS Program,” AIAA-2006-3080, 37th AIAA Plasmadynamics and Lasers Conference, San Francisco, CA, June 5-8, 2006.
- ³Thibodeaux, R., “Hypersonic Vehicle Electric Power Technology,” AIAA-2002-2109, 33rd AIAA Plasmadynamics and Lasers Conference, May 20-23, 2003.
- ⁴Dicks, J. B., and Scott, M. A., “The History and Future of Lightweight MHD Power Systems,” 20th IECEC, Miami Beach, FL, August 1985
- ⁵Lineberry J. T., Rosa R. J., Bityurin V. A., Bocharov A. N., and Potebnja V. G. “Prospects of MHD Flow Control for Hypersonics”, 35th Intersociety Energy Conversion Engineering Conference, AIAA 2000-3057, 24-28 July 2000, Las Vegas, NV.
- ⁶Sonju, O.K. and Tenoi, J., “Study of High Power, High Performance Portable MHD Power Supply Systems”, AFAPL-TR-76-87, August 1976.
- ⁷Swallow, D.W., et al., “Magnetohydrodynamic Lightweight Channel Development”, AFAPL-TR-78-41, June 1978
- ⁸Lineberry, J. T., Bityurin, V. A., and Litchford R. J., “Thermodynamic Analysis of the AJAX Propulsion Concept,” AIAA 2000-0445, 38th AIAA Aerospace Sciences Meeting, Reno, NV, January 2000.
- ⁹Macheret, S. O, et al, “Potential Performance of Supersonic MHD Power Generators”, AIAA 2001-0795, 39th AIAA Aerospace Sciences Meeting and Exhibit, Reno, NV, January 2001.
- ¹⁰Schmidt, H. J., et al., “Pulsed MHD Generator Development in the Soviet Union,” UTISI, 19th IECEC, 1984.
- ¹¹Velikov, E. P., et al., “Pulsed MHD Power System “Sakhalin” – The World Largest Solid Propellant Fueled MHD Generator of 500 MWe Electric Power Output,” Proceedings of the International Conference on MHD Power Generation and High Temperature Technologies, Beijing, China, October, 1999.
- ¹²Zeigarnik, V. A., et al., “The First Experiments with PAMIR 3U Pulsed Portable MHD Power System,” 33rd Symposium on Engineering Aspects of MHD, Tullahoma, TN, June 1995.
- ¹³Maxwell, C. D. and S. T. Demetriades, “Initial Tests of a Lightweight, Self-Excited MHD Power Generator,” AIAA Journal of Propulsion and Power, Vol.2, No. 3, pp 474-480, Sept-Oct, 1986.
- ¹⁴“Magnetohydrodynamic Energy Conversion”, Richard J. Rosa, McGraw-Hill, Inc., 1968.
- ¹⁵Wu, Y. C. L., “Performance Theory of Diagonal Conducting Sidewall MHD Generators,” AIAA Journal, Volume 4, No. 6, pp. 1362-1368, October, 1976.
- ¹⁶Lineberry, J. T., Lee, J. J., and Wu, Y. C. L., “Analysis of IEE Mark II MHD Generator Experiments”, AIAA-88-0724, AIAA 26th Aerospace Sciences Meeting, Reno, NV, January 1988.
- ¹⁷Lineberry, J. T., Wu, Y. C. L., and Nelson, G. L., “Analysis of Coal-Fired Generator Experiments at the CDIF,” Proceedings of the 28th Symposium on Engineering Aspects of Magnetohydrodynamics, Chicago, IL, June 1990.